# Supporting Information

**Interfacing RuO₂ with Pt to induce efficient charge transfer from Pt to RuO₂ for highly efficient and stable oxygen evolution under acidic media**

*Taehyun Kwon,[a,b†] Heesu Yang,[a,†] Minki Jun,[a] Taekyung Kim,[a] Jinwhan Joo,[a] Jun Kim,[b] Hionsuck Baik,[c] Jin Young Kim,[b] and Kwangyeol Lee[*, a]*

[a] Department of Chemistry and Research Institute for Natural Science, Korea University, Seoul 02841, Republic of Korea, E-mail: kylee1W@korea.ac.kr

[b] Center for Hydrogen Fuel Cell Research, Korea Institute of Science and Technology (KIST), Seoul 02792, Republic of Korea

[c] Seoul Center, Korea Basic Science Institute (KBSI), Seoul 02841, Republic of Korea

[†] These authors contributed equally on this work.

# Experimental Section

## Material Characterization

Transmission electron microscopy (TEM) and high-resolution TEM (HRTEM) were carried out on a TECNAI G2 20 S-Twin and a TECNAI G2 F30ST operated at 200 and 300 kV, respectively. High angle annular dark field scanning TEM (HAADF-STEM), energy dispersive X-ray spectroscopy (EDX) and aberration-corrected imaging and high-spatial-resolution EDX analyses were conducted on a FEI Titan Cubed 600-300 with Chemi-STEM technology and JEOL ARM200F Cs STEM. High-performance X-ray photoelectron spectroscopy (HP-XPS) was performed using K-ALPHA+XPS System developed by Thermo Fisher Scientific with spot size of 400 μm. The X-ray source was monochromatized Al-Kα ($hv$ = 1486.6 eV) at 72 W. Powder X-ray diffraction (PXRD) patterns were collected with a Rigaku Ultima III diffractometer system with a graphite monochromatized Cu-Kα radiation at 40 kV and 30 mA. Metal contents of the samples were analysed by inductively coupled plasma atomic emission spectroscopy (ICP-AES) analyser (700-ES, Varian).

## Electrochemical Measurements

Electrochemical measurements were conducted with an electrochemical workstation (CHI7007E, CH Instruments) at room temperature. A three-electrode system was built glassy carbon disk electrode (GCE), graphite rod, and Ag/AgCl (filled with saturated KCl) electrode as working, counter, and reference electrodes, respectively. All presented data were shown after conversion to the reversible hydrogen electrode (RHE) scale by measuring the open circuit potential (OCP) of Ag/AgCl reference electrode with RHE ($H^+|H_2$ equilibrium on the Pt electrode).

Before use, the GCE (Ø = 5 mm) was polished on a micro-cloth with a diamond (1 μm) suspension and alumina (0.05 μm) suspension. Catalyst ink (0.52 $mg_{Ru}$ $mL^{-1}$) was prepared by ultrasonication of slurry composed of the catalyst, IPA, deionized water, and 5 wt% Nafion (Nafion : catalyst mass ratio of 1 : 5) at least 30 min in an ice bath. The catalyst ink was drop-casted onto the GCE and spun at 700 rpm, and the electrode was dried at 60 ℃. The loading

amount of the catalysts on the electrode was controlled to be 20 $\mu g_{Ru}$ cm$^{-2}$. The GCE with the catalyst film was equipped on a rotation shaft of a rotating disk electrode (RRDE-3A, ALS) for electrochemical measurements.

Electrochemical cleaning before OER measurement was conducted by cyclic voltammetry (CV) in the potential range of 0.05 – 1.1 $V_{RHE}$ for 50 cycles at a scan rate of 500 mV s$^{-1}$ in N$_2$-saturated 0.1 M HClO$_4$. After electrochemical cleaning, OER polarization curve was obtained by a linear sweep voltammetry (LSV) in the potential range of 1.1 – 1.7 $V_{RHE}$ at a scan rate of 10 mV s$^{-1}$ in N$_2$-saturated 0.1 M HClO$_4$. All measurements were conducted with an electrode rotation at 1600 rpm and repeated at least three times. For *iR*-correction, solution resistance was measured by electrochemical impedance spectroscopy (EIS) performed at 1.4 $V_{RHE}$ from 10 kHz to 1 Hz with the potential amplitude of 10 mV s$^{-1}$. The presented data were 95% *iR*-corrected positive CV scans (manual *iR*-correction), by the *x*-intercept of the Nyquist plot in the high frequency region. For OER stability measurement, the working electrode was prepared on carbon fibre paper (Spectracarb, 2050A-0850, FuelCellStore) and the catalyst ink was drop-casted onto the carbon paper (1 × 1 cm$^2$, 100 $\mu g_{Ru}$ cm$^{-2}$). The OER stability of the catalysts was evaluated by chronopotentiometry (CP) at a constant current density of 10 mA cm$^{-2}$ in N$_2$-saturated 0.1 M HClO$_4$ electrolyte.

The electrochemical active surface area (ECSA) of the catalyst was measured from the double layer capacitance ($C_{dl}$) of the catalyst surface. The $C_{dl}$ was determined by measuring CVs at multiple scan rates in the non-Faradaic potential region. In this potential region, all measured currents were assumed to be associated with double-layer charging. In this work, CVs were measured in the potential range of 0.31 – 0.41 $V_{RHE}$ with the scan rates of 10, 20, 30, 40, 60, and 100 mV s$^{-1}$. As shown in equation (1), the measured charging current ($i_c$) is equal to the multiplication of scan rate ($v$) and the $C_{dl}$.

$$i_c = vC_{dl} \qquad (1)$$

The ECSA is derived from the equation (2) by dividing the $C_{dl}$, the slope derived from a plot of $i_c$ as a function of $v$, with specific capacitance ($C_s$).

$$ECSA = C_{dl} / C_s \qquad (2)$$

According to McCrory *et al.*,[S1] 0.035 mF cm$^{-2}$ of $C_s$ for 0.1 M HClO$_4$ was used to calculate ECSA.

**X-ray Absorption Spectroscopy (XAS)**

XAS on Ru K-edge, Pt L$_3$-edge, and Pt L$_2$-edge were performed at the beamline 7D of PLS-II, Pohang Accelerator Laboratory (PAL) in Republic of Korea. X-ray was monochromatized by double crystal monochromator with Si (111) crystals for the energy scan. Measurement was conducted in transmission-fluorescence geometry, where the spectra were obtained by fluorescence mode at room temperature. For data calibration, spectra of the reference metal foils placed behind the sample were simultaneously, measured in transmission mode. The Ru K-edge, Pt L$_3$-edge, and Pt L$_2$-edge XAS spectra were calibrated 22117, 11564, and 13273 eV, respectively, by the reference metal foils. The obtained XAS raw data was processed by the ATHENA program.[S2]

# Supporting Tables S1 to S5

**Table S1.** Summary of relative peak areas of Pt species calculated from Pt 4f XPS spectra of the catalysts.

| Catalyst | $Pt^0$ (%) $4f_{7/2} = 71.5 \pm 0.1$ eV $4f_{5/2} = 74.9 \pm 0.1$ eV | $Pt^{2+}$ (%) $4f_{7/2} = 72.4 \pm 0.1$ eV $4f_{5/2} = 75.8 \pm 0.1$ eV | $Pt^{4+}$ (%) $4f_{7/2} = 74.9 \pm 0.1$ eV $4f_{5/2} = 78.3 \pm 0.1$ eV |
|---|---|---|---|
| D-NW | 100 | 0 | 0 |
| D-NW-a | 79.4 | 13.7 | 6.9 |
| D-NW-a after OER | 59.8 | 28.0 | 12.2 |
| C-NW | 100 | 0 | 0 |
| C-NW-a | 79.9 | 15.8 | 4.3 |
| C-NW-a after OER | 77.3 | 22.0 | 0.7 |
| A-NW | 100 | 0 | 0 |
| A-NW-a | 80.1 | 15.8 | 4.1 |
| A-NW-a after OER | 76.9 | 16.1 | 7.0 |

**Table S2.** Summary of relative peak areas of Ru species calculated from the Ru $3p_{3/2}$ XPS spectra of the catalysts.

| Catalyst | $Ru^0$ (%) $3p_{3/2} = 461.2 \pm 0.1$ eV | $Ru^{3+}$ (%) $3p_{3/2} = 461.2 \pm 0.1$ eV | $Ru^{4+}$ (%) $3p_{3/2} = 461.2 \pm 0.1$ eV $Satellite = 465.4 \pm 0.1$ eV |
|---|---|---|---|
| D-NW | 36.7 | 8.4 | 54.9 |
| D-NW-a | 8.1 | 13.4 | 78.5 |
| D-NW-a after OER | 5.2 | 15.6 | 79.2 |
| C-NW | 36.5 | 5.3 | 58.2 |
| C-NW-a | 8.3 | 10.3 | 81.4 |
| C-NW-a after OER | 5.5 | 12.3 | 82.2 |
| A-NW | 36.6 | 5.1 | 58.3 |
| A-NW-a | 9.7 | 12.1 | 78.2 |
| A-NW-a after OER | 5.5 | 15.0 | 79.5 |

**Table S3.** Summary of relative peak areas of O species calculated from the O 1s XPS spectra of the catalysts.

| Catalyst | Lattice O (%) $1s = 530.1 \pm 0.2$ eV | –OH (%) $1s = 531.8 \pm 0.2$ eV | H$_2$O (%) $1s = 533.5 \pm 0.3$ eV |
|---|---|---|---|
| D-NW-a | 9.7 | 21.2 | 62.2 |
| D-NW-a after OER | 7.0 | 28.1 | 60.6 |
| C-NW-a | 0 | 15.1 | 84.9 |
| C-NW-a after OER | 0 | 20.8 | 79.2 |
| A-NW-a | 0 | 38.0 | 62.0 |
| A-NW-a after OER | 0 | 23.8 | 76.2 |

**Table S4.** ICP-AES analysis results for the metal contents in the catalysts.

| Catalyst | Au (wt%) | Pt (wt%) | Ru (wt%) | Total metal contents (wt%) |
|---|---|---|---|---|
| D-NW/C | 2.52 | 2.45 | 3.56 | 8.53 |
| C-NW/C | 5.72 | 4.92 | 2.31 | 12.95 |
| A-NW/C | 5.56 | 6.10 | 2.21 | 13.86 |
| D-NW-a | 4.42 | 4.69 | 1.80 | 10.91 |
| C-NW-a | 6.62 | 5.61 | 2.24 | 14.47 |
| A-NW-a | 8.45 | 8.68 | 2.45 | 13.58 |

**Table S5.** Comparison of the performance of Ru-based electrocatalysts for the OER under acidic media.

| Catalyst | Electrolyte | Mass Loading (μg cm$^{-2}$) | $\eta_{10}$ (mV)[a] | Mass activity (A mg$^{-1}$) | Tafel slope (mV dec$^{-1}$) | Stability (CP[b] / ADT[c]) | Ref. |
|---|---|---|---|---|---|---|---|
| D-NW-a | 0.1 M HClO$_4$ | 20 (Ru) 121 (Ru+Pt+Au) | 215 | 1.31 (Ru) 0.216 (Ru+Pt+Au) @ 1.48 V$_{RHE}$ | 59.2 | > 40 h @ 10 mA cm$^{-2}$ | This work |
| A-NW-a | 0.1 M HClO$_4$ | 20 (Ru) 111 (Ru+Pt+Au) | 243 | 0.63 (Ru) 0.113 (Ru+Pt+Au) @ 1.48 V$_{RHE}$ | 54.7 | ~ 11 h @ 10 mA cm$^{-2}$ | This work |
| C-NW-a | 0.1 M HClO$_4$ | 20 (Ru) 130 (Ru+Pt+Au) | 254 | 0.46 (Ru) 0.071 (Ru+Pt+Au) @ 1.48 V$_{RHE}$ | 87.2 | ~ 7 h @ 10 mA cm$^{-2}$ | This work |
| h-PNRO/C | 0.1 M HClO$_4$ | 14 (Ru+Pt) | 239 | 4.28 (Ru+Pt) @ 1.53 V$_{RHE}$ | 52 | 91.1% MA[d] after 2k cycles | S3 |
| Ru$_1$-Pt$_3$Cu | 0.1 M HClO$_4$ | 16.3 (Ru+Pt) | 220 | 0.779 (Ru+Pt) @ 1.51 V$_{RHE}$ | - | > 28 h @ 10 mA cm$^{-2}$ | S4 |
| Ru$_{0.9}$Pt$_{0.1}$O$_2$/C | 0.05 M H$_2$SO$_4$ | 24.6 (Ru+Pt) | 248 | - | - | > 40 h @ 1 mA cm$^{-2}$ | S5 |
| AuRu branched NPs | 0.1 M HClO$_4$ | 408 (Ru+Au) | 220 | - | 47 | - | S6 |
| PdO@RuO$_2$- 4 layers | 0.1 M HClO$_4$ | 40 (Ru+Pd) | 257 | - | 66 | 95% TOF[e] after 2k cycles | S7 |
| RuRh@(RuRh)O$_2$ | 0.1 M HClO$_4$ | 20.4 (Ru+Rh) | 245 | 0.12 (Ru+Rh) @ 1.48 V$_{RHE}$ | 51.2 | ~ 2 h @ 5 mA cm$^{-2}$ | S8 |
| CIS@Ir$_{48}$Ru$_{52}$ | 0.1 M HClO$_4$ | 12 (Ru+Ir) | 244 | - | 57.6 | > 100 h @ 5 mA cm$^{-2}$ | S9 |
| Co-RuIr | 0.1 M HClO$_4$ | 50.9 (Ru+Ir) | 235 | - | 66.9 | ~ 25 h @ 10 mA cm$^{-2}$ | S10 |
| Ru@IrO$_x$ | 0.05 M H$_2$SO$_4$ | 362.7 (Ru+Ir) | 282 | 0.645 (Ru+Ir) @ 1.56 V$_{RHE}$ | 69.1 | ~ 24 h @ 10 mA cm$^{-2}$ | S11 |
| IrRu@Te | 0.5 M H$_2$SO$_4$ | 150 (Ru+Ir) | 220 | 0.59 (Ru+Ir) @ 1.5 V$_{RHE}$ | 35 | 20 h @ 10 mA cm$^{-2}$ | S12 |
| RuNi$_2$@G-250 | 0.5 M H$_2$SO$_4$ | 320 (catal.) | 227 | 0.058 (catal.) @ 1.48 V$_{RHE}$ | 65 | ~ 24 h @ 10 mA cm$^{-2}$ | S13 |
| RuO$_x$ nanosheets | 0.1 M HClO$_4$ | 200 (Ru) | 255 | 0.042 (Ru) @ 1.47 V$_{RHE}$ | 38 | ~ 6 h @ 10 mA cm$^{-2}$ | S14 |

[a] Overpotential to drive current density of 10 mA cm$^{-2}$, [b] Chronopotentiometry at a certain current density, [c] Accelerated durability test, [d] mass activity, [e] turnover frequency

**Table S6.** Summary of fitting parameter for EIS Nyquist plot at 1.4 $V_{RHE}$ in Fig. 4d of the catalysts in 0.1 M HClO$_4$.

| Catalyst | $R_{sol}$ [$\Omega$] | $R_{ct}$ [$\Omega$] | $C_{dl}$ [mF] |
|---|---|---|---|
| D-NW-a | 35.1 | 10.7 | 4.66 |
| C-NW-a | 30.6 | 17.8 | 3.62 |
| A-NW-a | 33.1 | 32.2 | 3.01 |
| RuO$_2$/C | 48.1 | 664.8 | 3.06 |

## Supporting Video S1

**Video S1.** Video of bubble generation during OER stability test of D-NW-a catalyst.

# Supporting Figs. S1 to S39 and Notes S1 to S5.
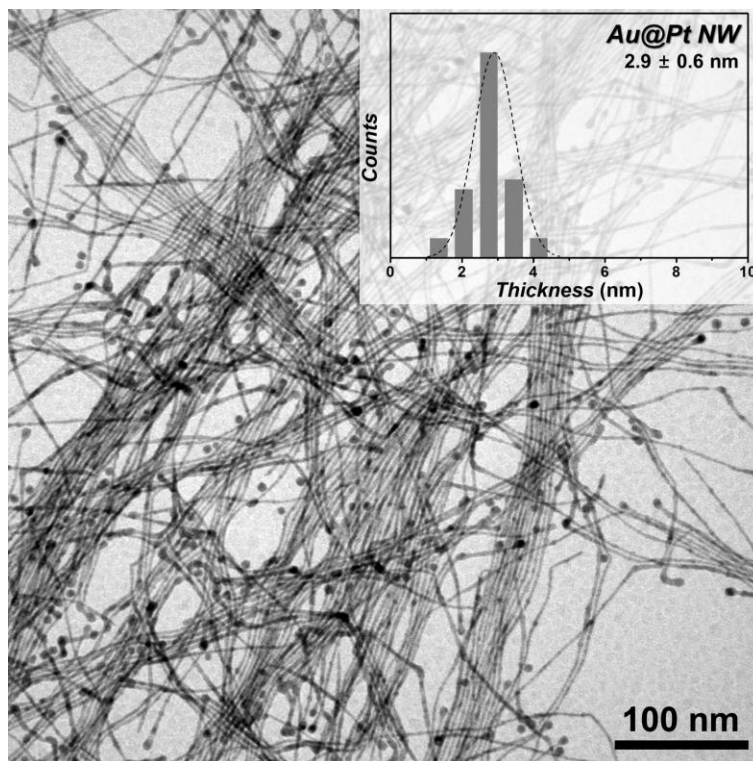


**Fig. S1.** TEM image of core@shell Au@Pt nanowires (Au@Pt NWs). Histogram in the inset represents the thickness distribution of Au@Pt NWs.
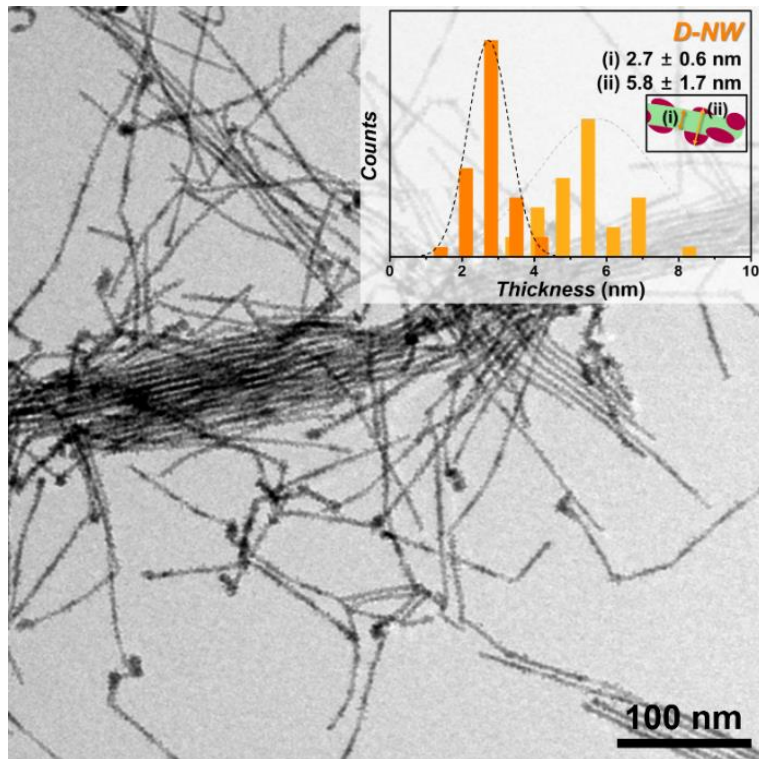
**Fig. S2.** Low magnification TEM image of D-NWs. Histogram in the inset represents the thickness distribution of D-NWs; (i) wire part only and (ii) sum of wire and patchy dendrite part.
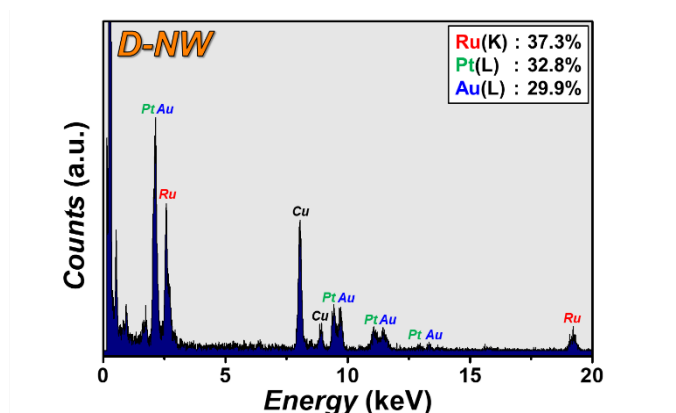
**Fig. S3.** EDX spectrum of D-NWs. Signals of Cu contents are detected from Cu TEM grid.
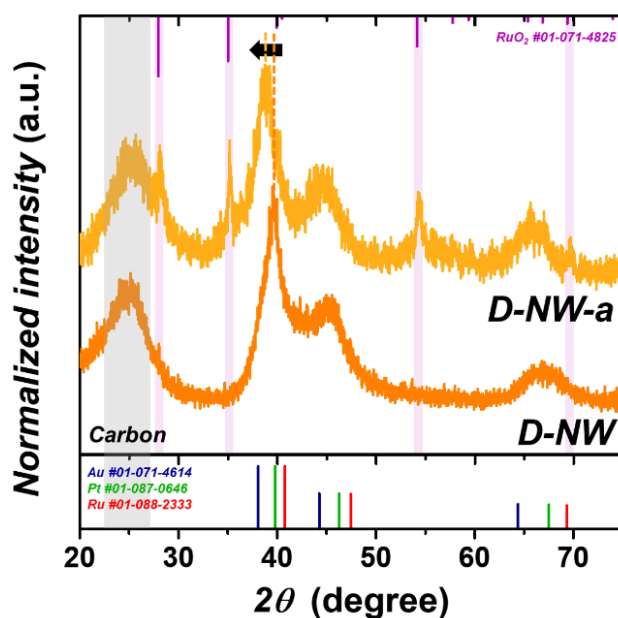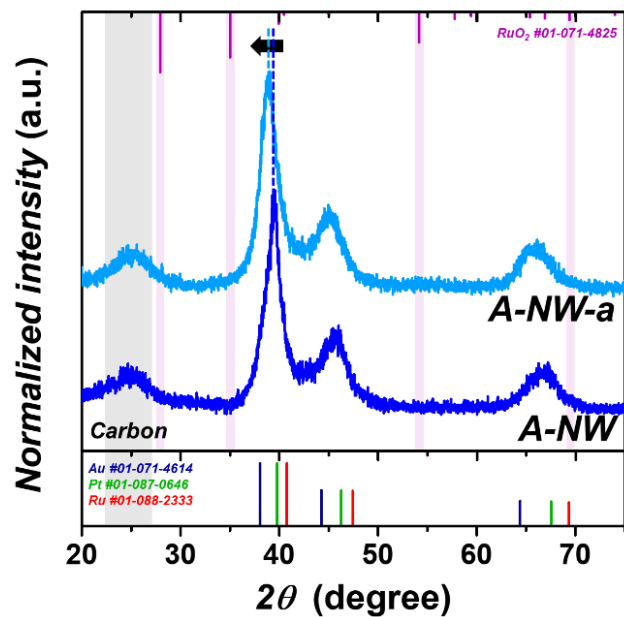


**Fig. S4.** PXRD patterns of D-NW and D-NW-a. Broad peaks near 25o in D-NW and D-NW-a are originated from carbon support (VC-XC72R). The colour bars indicate the PXRD line for the JCPDS references: Au (blue, #01-071-4614), Pt (green, #01-087-0646), fcc Ru (red, #01-088-2333), and rutile RuO2 (purple, #01-071-4825).
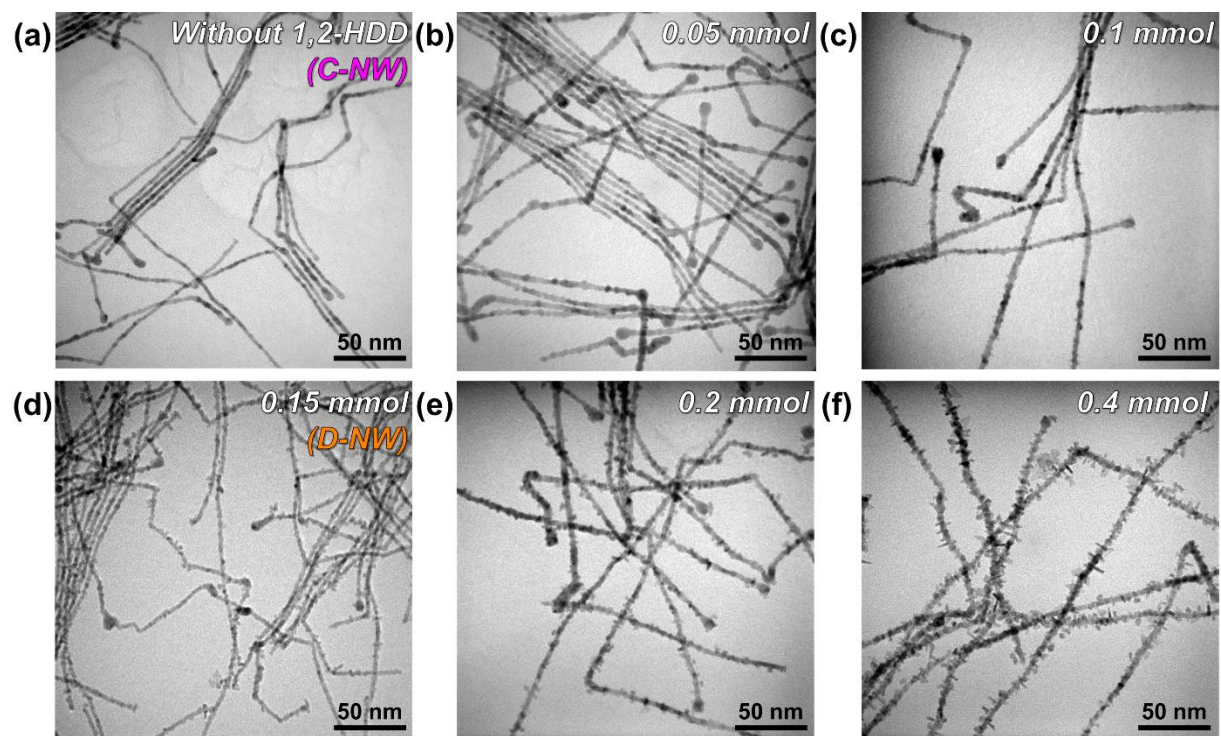
**Fig. S5.** TEM images of Au@Pt@Ru NWs by using different amount of 1,2-HDD; (a) without 1,2-HDD (C-NWs), (b) 0.05 mmol, (c) 0.1 mmol, (d) 0.15 mmol (D-NWs), (e) 0.2 mmol, and (f) 0.4 mmol.
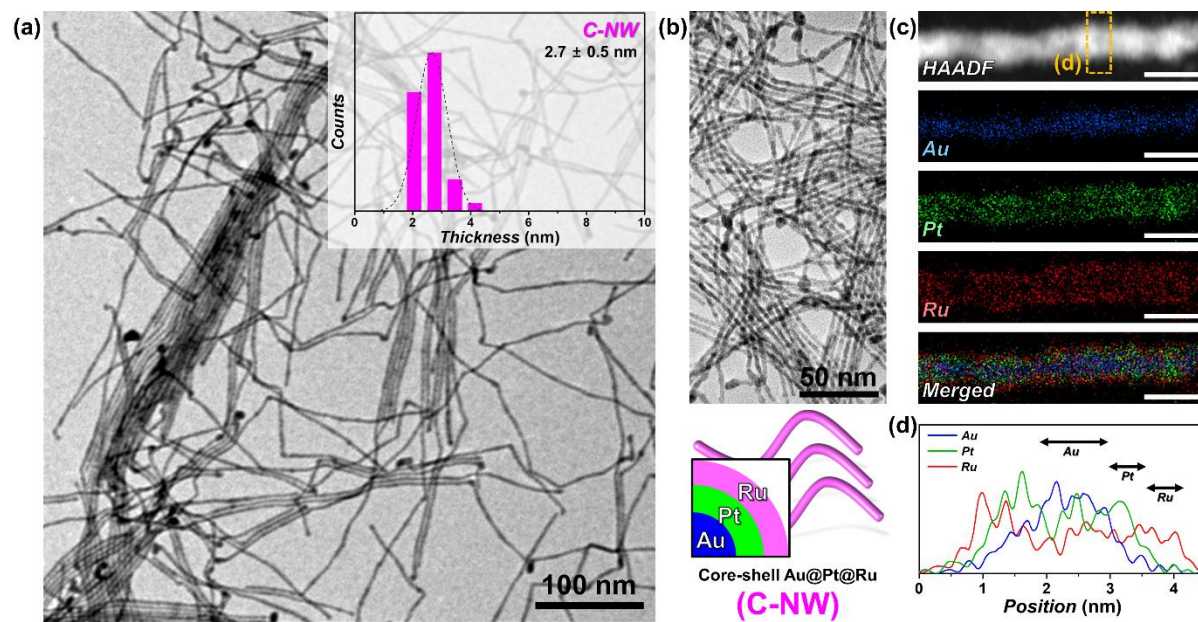
**Fig. S6.** Structure characterization of C-NWs. (a) Low magnification TEM image of C-NWs. Histogram in the inset represents the thickness distribution of C-NWs. (b) TEM image and schematic illustration of C-NWs. (c) HAADF-STEM image and corresponding elemental mapping analysis of Au (blue), Pt (green), and Ru (red) content in C-NW. Scale bar = 10 nm. (d) EDX line profile analysis of C-NW of marked area in the panel (c).
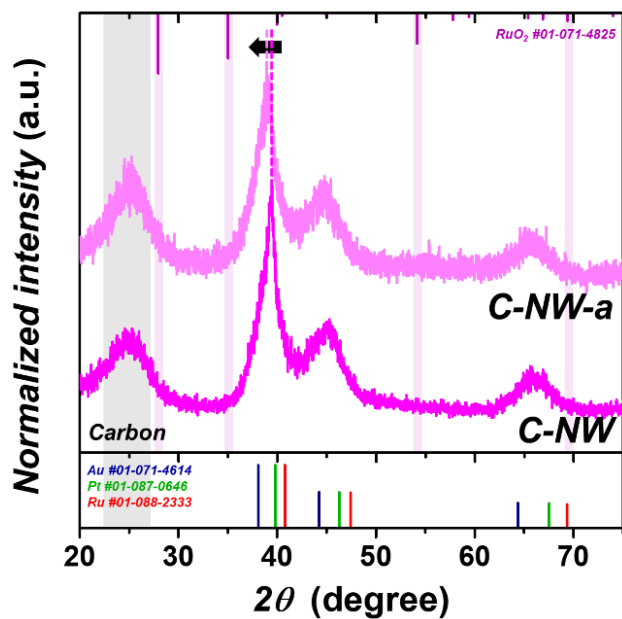
**Fig. S7.** PXRD patterns of C-NW and C-NW-a. Broad peaks near 25° in C-NW and C-NW-a are originated from carbon support (VC-XC72R). The colour bars indicate the PXRD line for the JCPDS references: Au (blue, #01-071-4614), Pt (green, #01-087-0646), fcc Ru (red, #01-088-2333), and rutile RuO2 (purple, #01-071-4825).
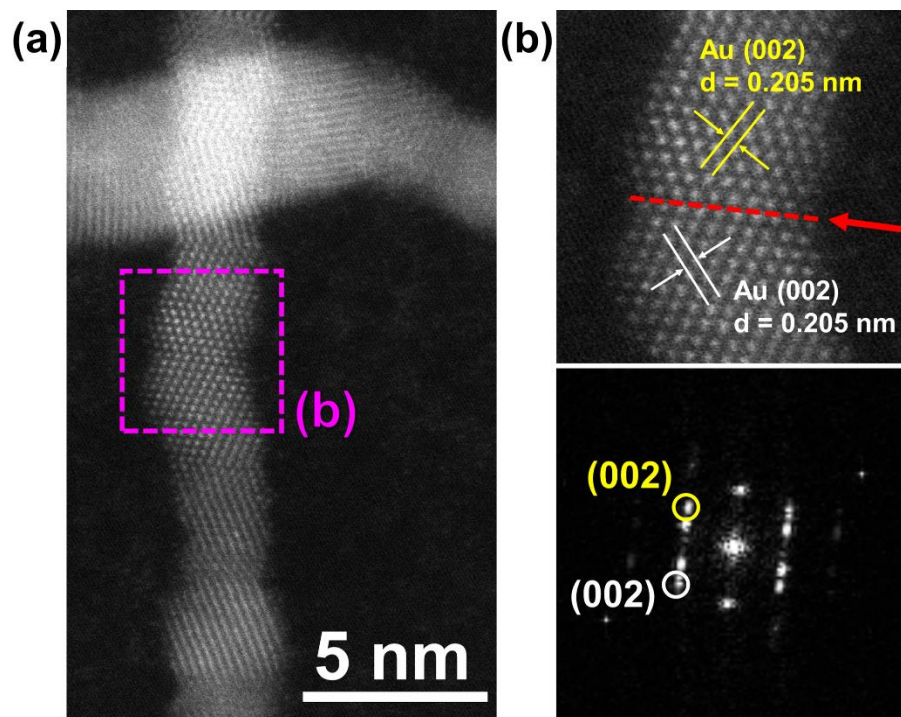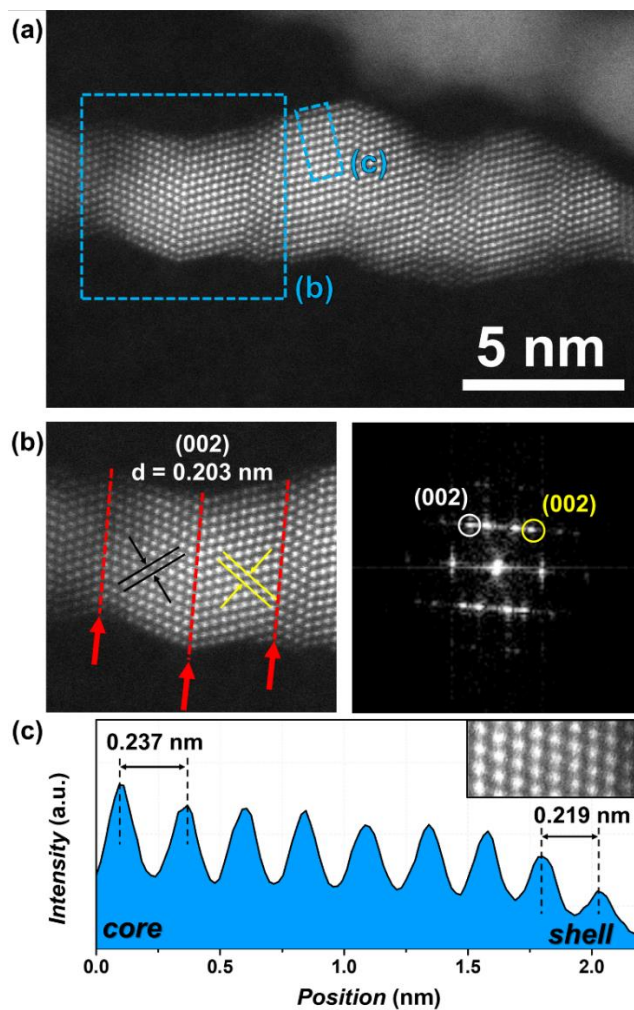
**Fig. S8.** (a) HR-STEM image of C-NW. (b) Enlarged HR-STEM image of marked area in the panel (a) and corresponding FFT pattern.

**Note S1.** *HR-STEM analysis of C-NW.* The HR-STEM image and corresponding FFT pattern of C-NWs **(Fig. S8)** indicated that the measured lattice spacing of 0.205 nm corresponds to the (002) facet of *fcc* Au at the core. Moreover, the twinning boundaries were also observed (Red dotted line), originating from the Au@Pt NW.
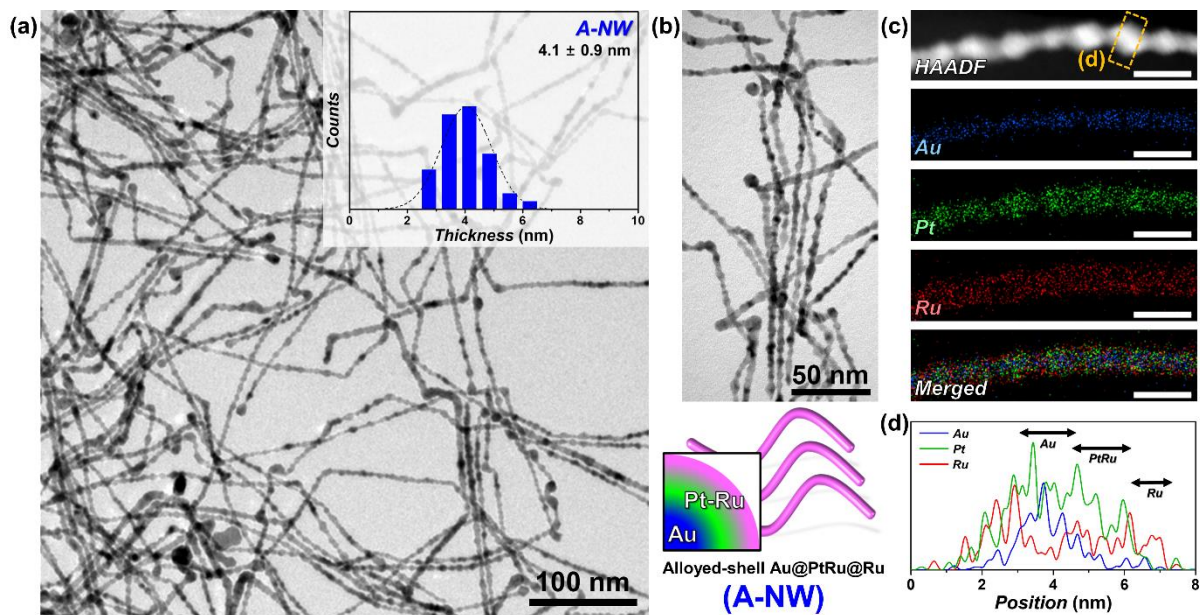
**Fig. S9.** Structure characterization of A-NWs. (a) Low magnification TEM image of A-NWs. Histogram in the inset represents the thickness distribution of A-NWs. (b) TEM image and schematic illustration of A-NWs. (c) HAADF-STEM image and corresponding elemental mapping analysis of Au (blue), Pt (green), and Ru (red) content in A-NW. Scale bar = 10 nm. (d) EDX line profile analysis of A-NW of marked area in the panel (c).

**Fig. S10.** PXRD patterns of A-NW and A-NW-a. Broad peaks near 25$^{\circ}$ in A-NW and A-NW-a are originated from carbon support (VC-XC72R). The colour bars indicate the PXRD line for the JCPDS references: Au (blue, #01-071-4614), Pt (green, #01-087-0646), fcc Ru (red, #01-088-2333), and rutile $RuO_2$ (purple, #01-071-4825).

**Fig. S11.** (a) HR-STEM image of A-NW. (b) Enlarged HR-STEM image of marked area in the panel (a) and corresponding FFT pattern. (c) HAADF-STEM intensity profile taken from the area in the panel (a).

**Note S2.** *HR-STEM analysis of A-NW.* The HR-STEM image and corresponding FFT pattern of A-NWs **(Fig. S11)** indicated that the measured lattice spacing of 0.203 nm corresponds to the (002) facet of *fcc* phase at the core, which is slightly smaller than that of *fcc* Au phase. Moreover, the twinning boundaries were also observed (Red dotted line), indicating similar crystallographic feature of A-NW with D-NW and C-NW. However, by the HAADF-STEM intensity profile **(Fig. S11c)**, the lattice distances of (111) *fcc* facet decrease from 0.237 nm to 0.219 nm, from core to the shell of A-NW. The lattice spacing of 0.237 nm corresponds to the lattice spacing of Au(111), whereas the lattice spacing of 0.219 nm is larger than Ru(111) but smaller than Pt(111), indicating that the shell consists of PtRu alloy.

18
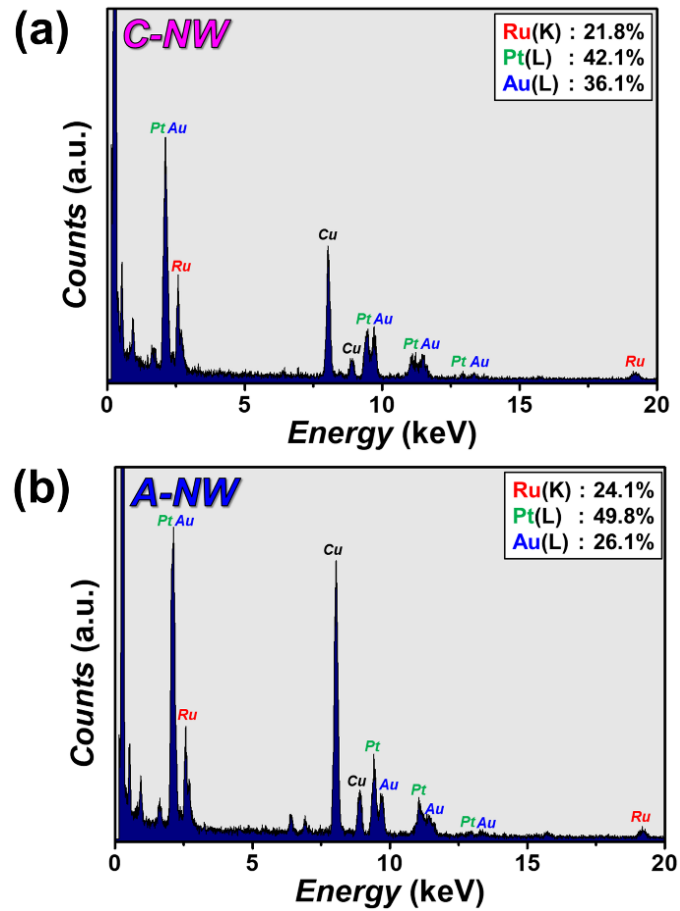
**Fig. S12.** EDX spectra of (a) C-NWs and (b) A-NWs. Signals of Cu contents are detected from Cu TEM grid.
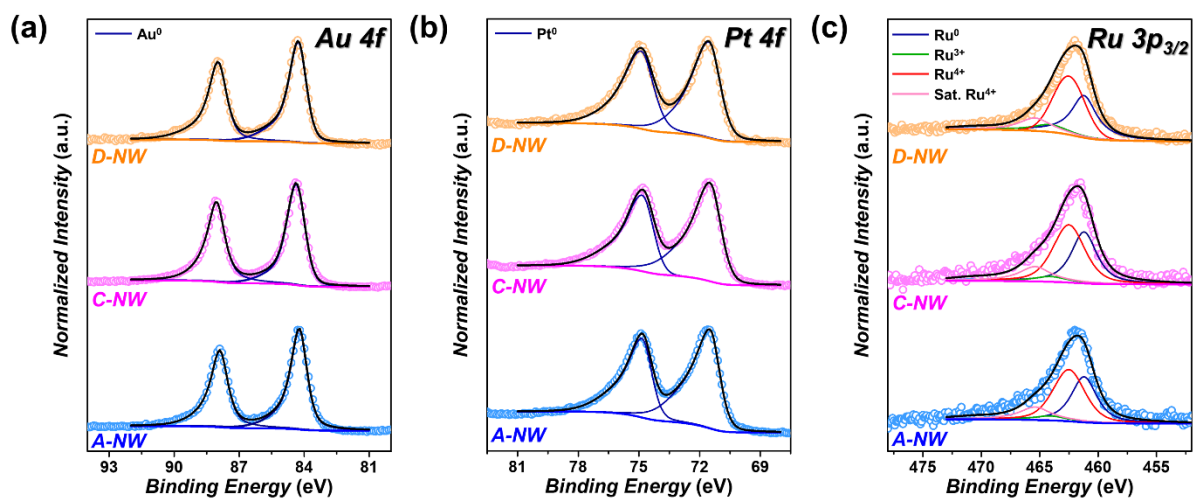
**Fig. S13.** (a) Au 4f, (b) Pt 4f, and (c) Ru $3p_{3/2}$ XPS spectra of D-NW, C-NW, and A-NW.
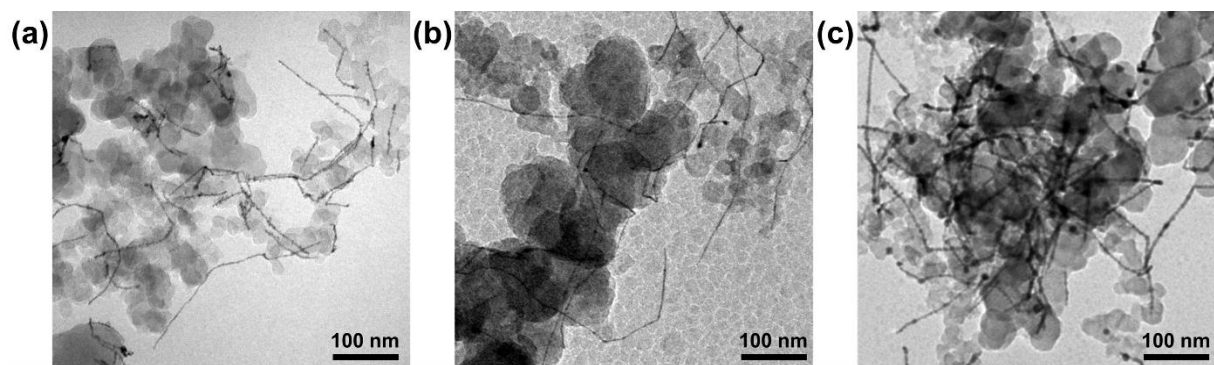


**Fig. S14.** TEM images of (a) D-NW/C, (b) C-NW/C, and (c) A-NW/C.
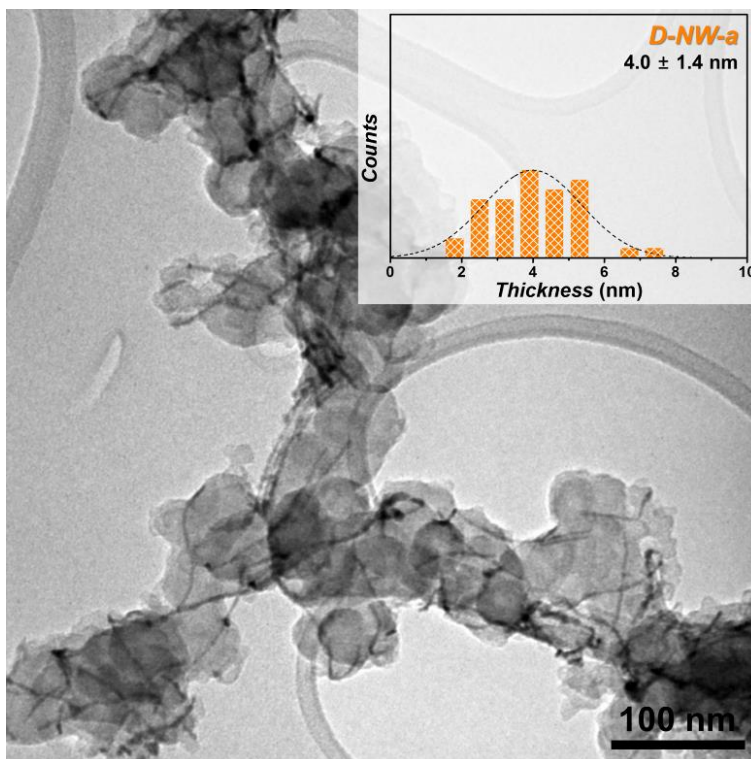
**Fig. S15.** Low magnification TEM image of D-NW-a. Histogram in the inset represents the thickness distribution of D-NW-a.
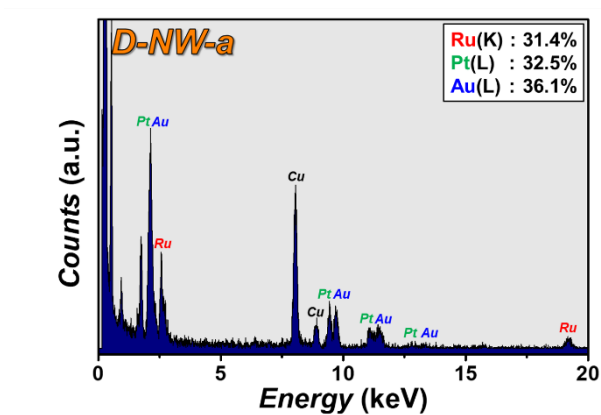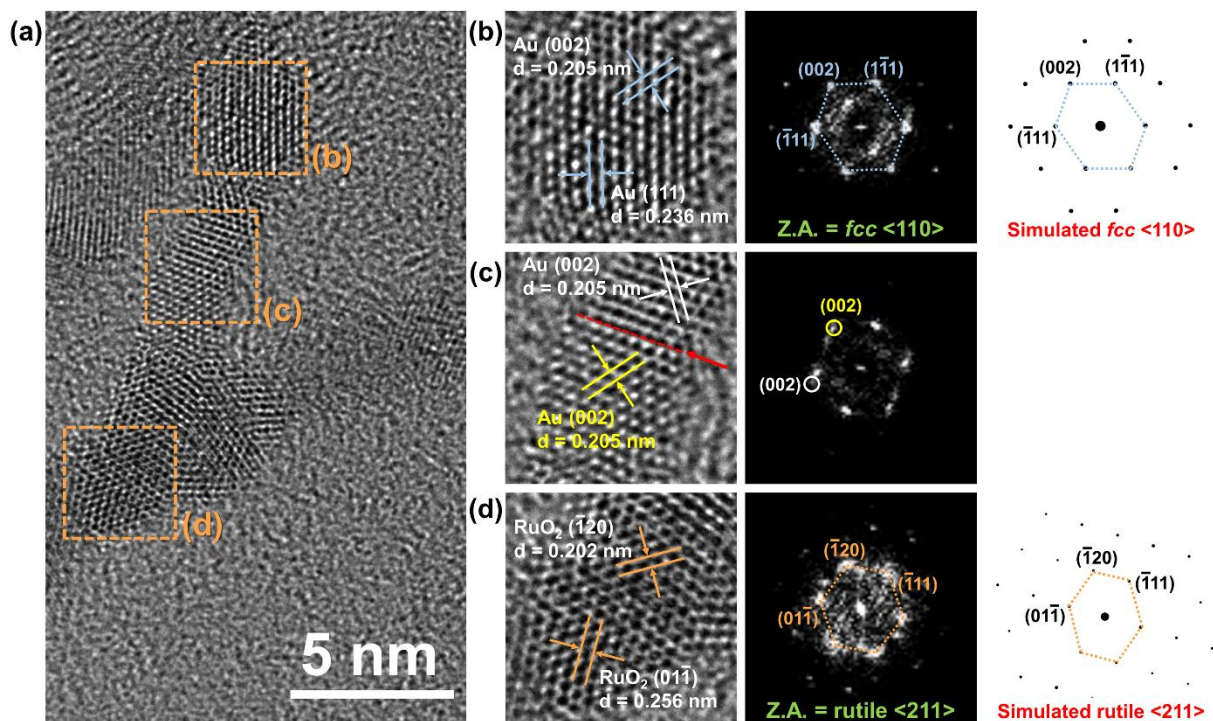


**Fig. S16.** EDX spectra of D-NW-a. Signals of Cu contents are detected from Cu TEM grid.

**Fig. S17.** (a) HRTEM image of D-NW-a. (b-d) Enlarged HRTEM images of D-NW-a of the marked area in the panel (a) and corresponding FFT patterns: (b-c) fcc phase wire part, and (d) protruded rutile $RuO_2$ part.

**Note S3.** *HRTEM analysis of D-NW-a.* The HRTEM image **(Fig. S17)** exhibited the crystallographic features of wire part **(Fig. S17a-c)** and dendrite part **(Fig. S17d)** in D-NW-a. The measured distances of 0.205 and 0.236 nm in Fig. S17b-c correspond to Au(002) and Au(111) facets, respectively, observed from the zone axis of *fcc* <110>. Moreover, the twinned features in wire part were maintained **(Fig. S17)**, which were observed from D-NW **(Fig. 1d-f)**. On the other hand, the measured distances of 0.256 and 0.202 nm correspond to $(\bar{1}20)$ and $(01\bar{1})$ facets of rutile $RuO_2$ phase, observed from the zone axis of <211>.
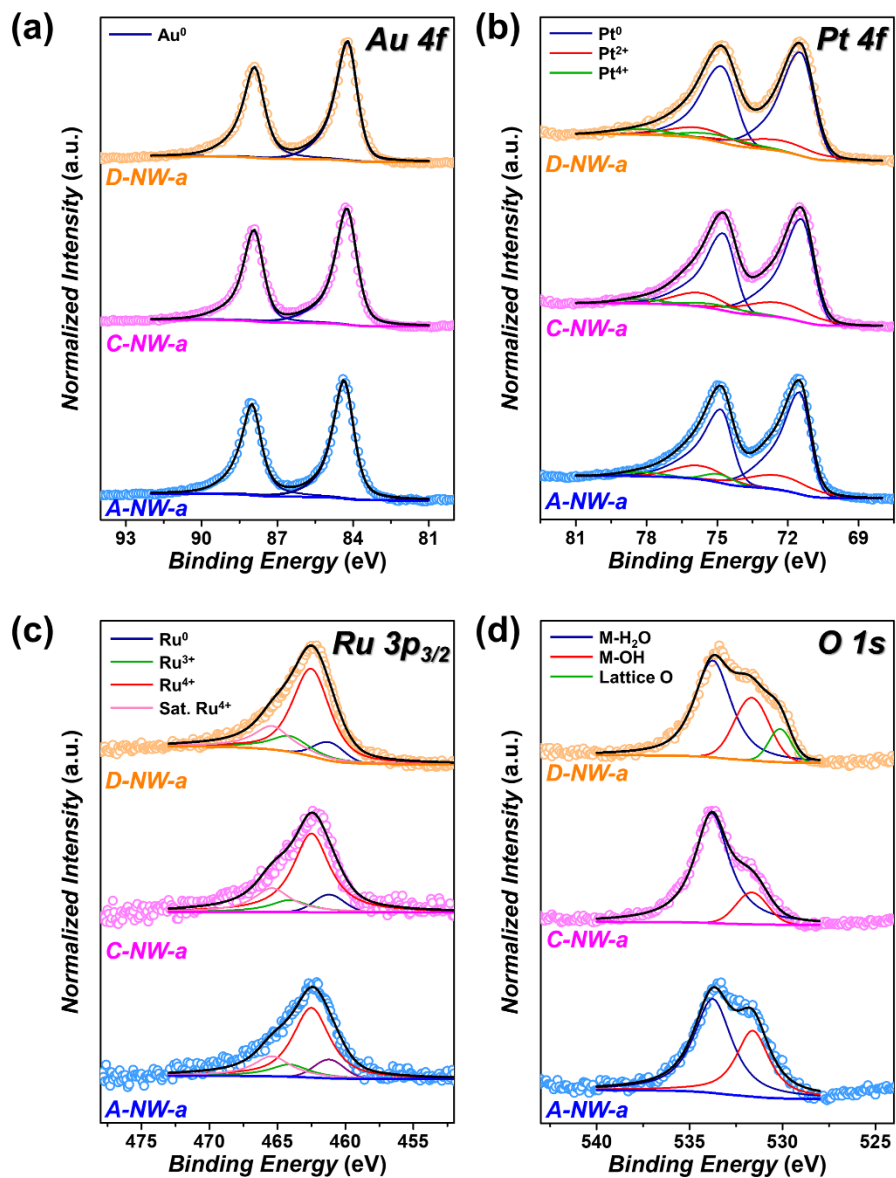
**Fig. S18.** (a) Au 4f, (b) Pt 4f, (c) Ru 3p$_{3/2}$, and (d) O 1s XPS spectra of D-NW-a, C-NW-a, and A-NW-a.
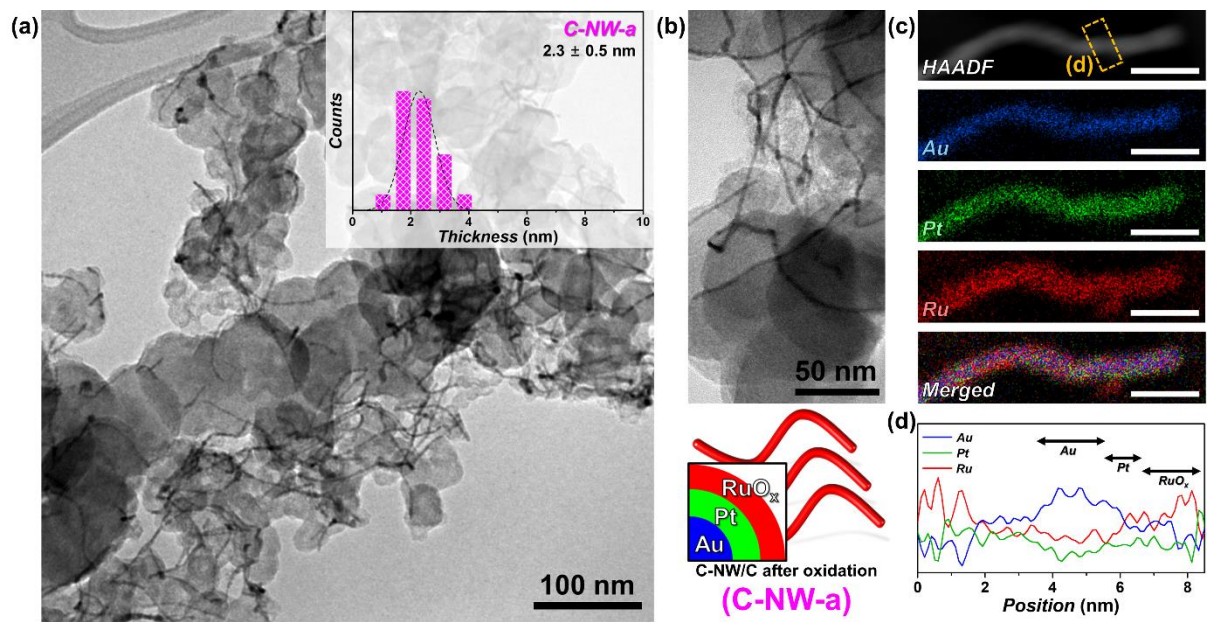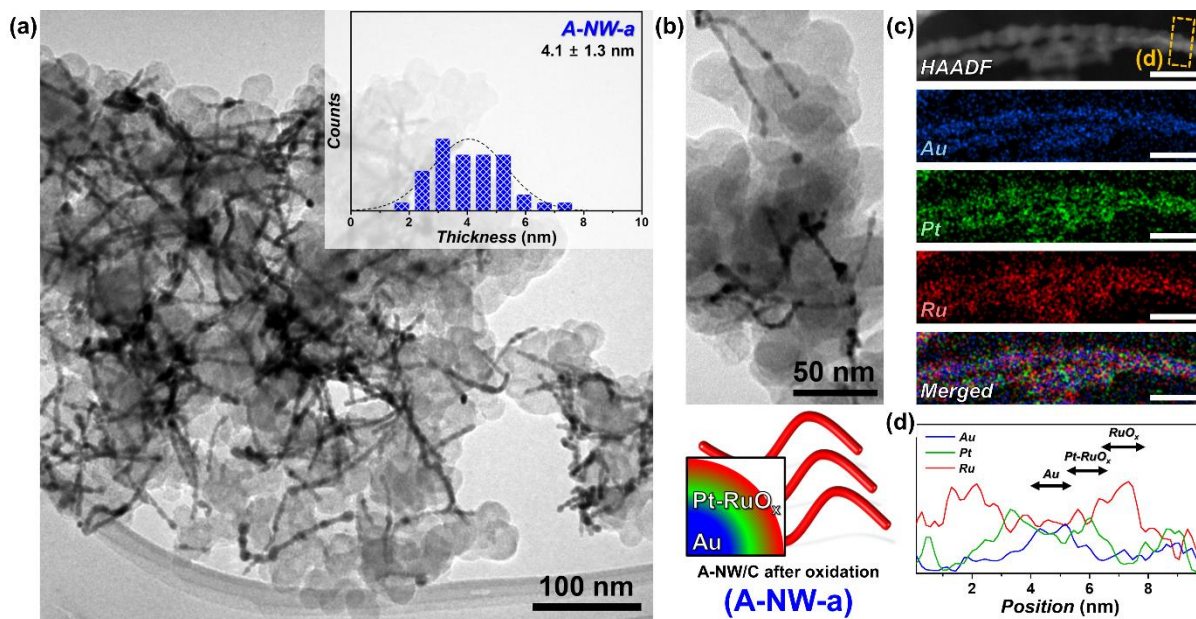
**Fig. S19.** Structure characterization of C-NW-a. (a) Low magnification TEM image of C-NW-a. Histogram in the inset represents the thickness distribution of C-NW-a. (b) TEM image and schematic illustration of C-NW-a. (c) HAADF-STEM image and corresponding elemental mapping analysis of Au (blue), Pt (green), and Ru (red) content in C-NW-a. Scale bar = 10 nm. (d) EDX line profile analysis of C-NW-a of marked area in the panel (c).
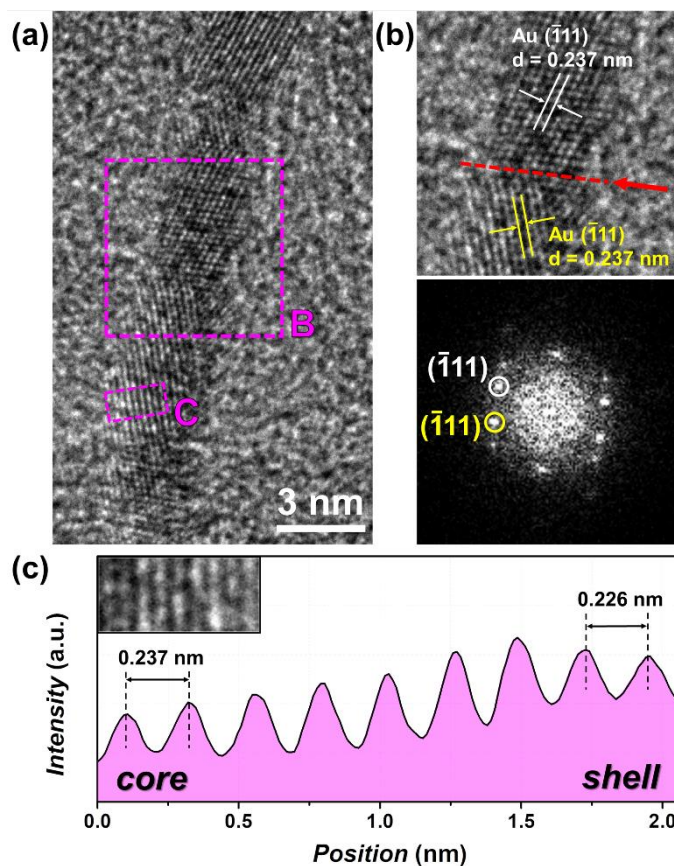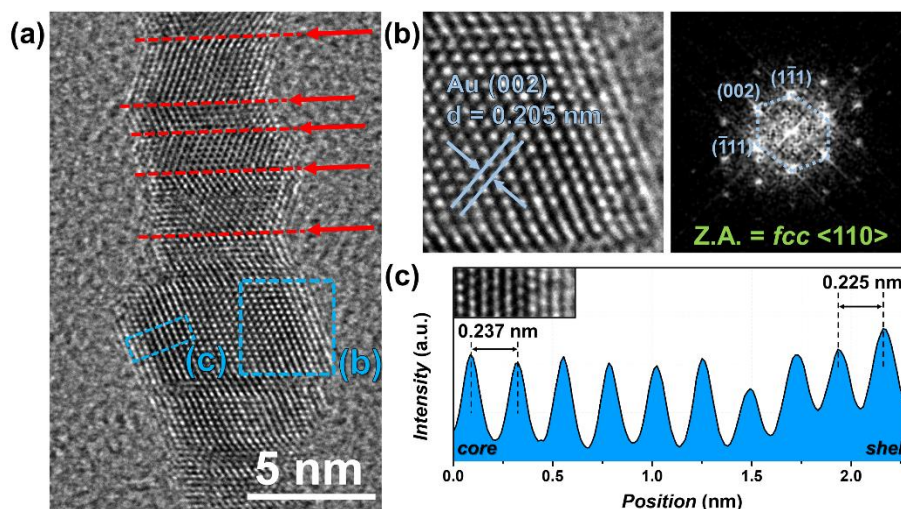
**Fig. S20.** (a) HRTEM image of C-NW-a. (b) Enlarged HRTEM image of marked area in the panel (a) and corresponding FFT pattern. (c) Intensity profile taken from the area in the panel (a).

**Note S4.** *HRTEM analysis of C-NW-a.* The HRTEM image of C-NW-a **(Fig. S20)** and corresponding FFT patterns revealed that the measured lattice spacing of 0.237 nm at the core corresponds to the Au($\bar{1}$11) facet. Also, the twinned feature observed in C-NW is still observed in C-NW-a as shown in the red dotted line in the **Fig. S20b**. Moreover, the intensity profile (Fig. S20c) exhibited that the lattice distances of ($\bar{1}$11) facets decreased from 0.237 to 0.226 nm from the core to the shell of C-NW-a. The lattice spacing of 0.237 nm corresponds to the lattice spacing of Au($\bar{1}$11), whereas the lattice spacing of 0.226 nm corresponds to the lattice spacing of Pt($\bar{1}$11), indicating the Au@Pt core@shell structure. However, crystallographic feature of rutile $RuO_2$ was not observed, indicating the formation of amorphous $RuO_x$.

**Fig. S21.** Structure characterization of A-NW-a. (a) Low magnification TEM image of A-NW-a. Histogram in the inset represents the thickness distribution of A-NW-a. (b) TEM image and schematic illustration of A-NW-a. (c) HAADF-STEM image and corresponding elemental mapping analysis of Au (blue), Pt (green), and Ru (red) content in A-NW-a. Scale bar = 10 nm. (d) EDX line profile analysis of A-NW-a of marked area in the panel (c).

**Fig. S22.** (a) HRTEM image of A-NW-a. (b) Enlarged HRTEM image of marked area in the panel (a) and corresponding FFT pattern. (c) Intensity profile taken from the area in the panel (a).

**Note S5.** *HRTEM analysis of A-NW-a.* The HRTEM image of A-NW-a **(Fig. S22)** and corresponding FFT patterns revealed that the measured lattice spacing of 0.205 nm at the core corresponds to the Au(002) facet. Also, the twinned feature observed in A-NW is still observed in A-NW-a as shown in the red dotted line in the **Fig. S22a**. Moreover, the intensity profile **(Fig. S22c)** exhibited that the lattice distances of ($\bar{1}$11) facets decreased from 0.237 to 0.225 nm from the core to the shell of C-NW-a. The lattice spacing of 0.237 nm corresponds to the lattice spacing of Au($\bar{1}$11), whereas the lattice spacing of 0.225 nm corresponds to the lattice spacing of Pt($\bar{1}$11), but which is slightly smaller than that of C-NW-a **(Fig. S20c)**, indicating the alloyed surface of the shell. Moreover, the measured lattice spacing of 0.225 nm of the shell is slightly larger than that of A-NW of 0.219 nm **(Fig. S11c)**, indicating the oxidation of metallic *fcc* Ru phase, which is in accordance with the PXRD patterns **(Fig. S10)**. However, crystallographic feature of rutile $RuO_2$ was not observed, indicating the formation of amorphous $RuO_x$.
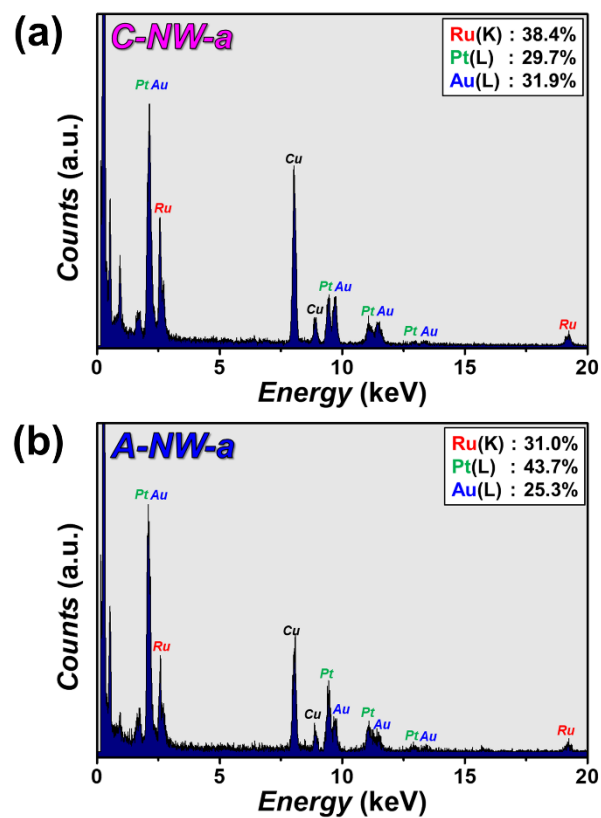
**Fig. S23.** EDX spectra of (a) C-NW-a and (b) A-NW-a. Signals of Cu contents are detected from Cu TEM grid.
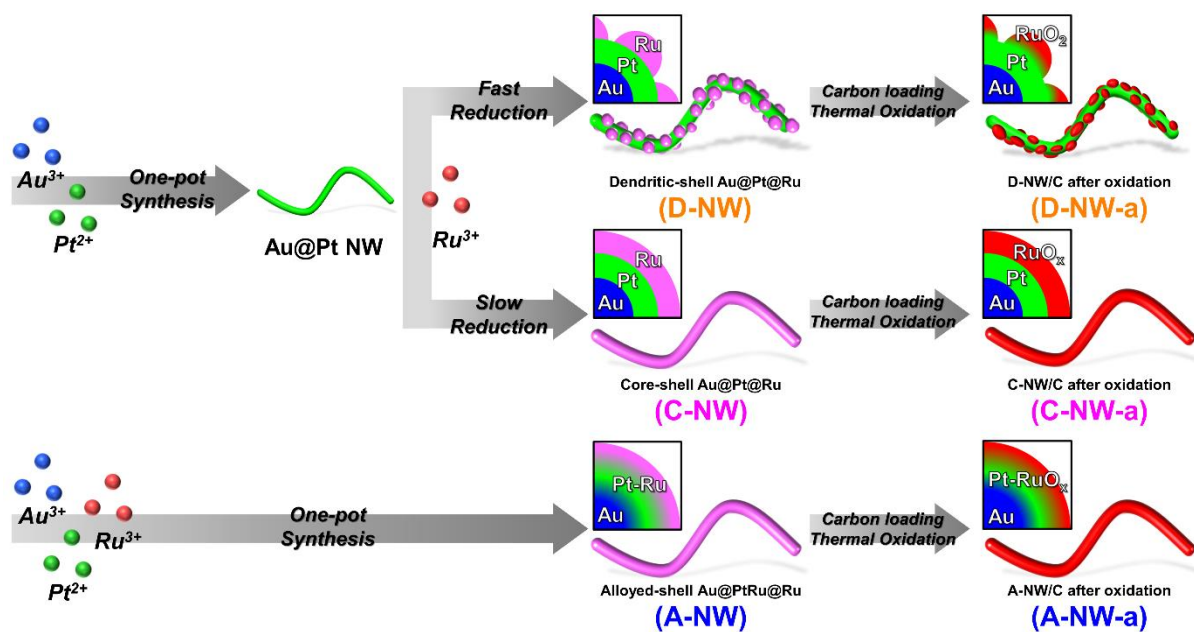
**Fig. S24.** Schematic illustration of overall synthetic scheme of three types of Au@Pt@Ru NW and NW-a catalysts.
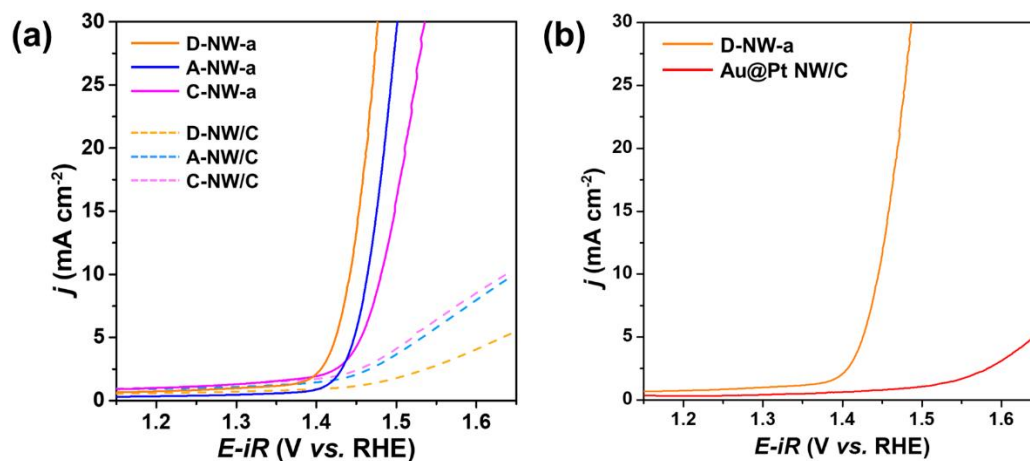


**Fig. S25.** OER polarization curves of (a) three NW-a (after thermal oxidation) and three NW/C (before thermal oxidation) catalysts and (b) Au@Pt NW/C catalyst measured in $N_2$-saturated 0.1 M $HClO_4$.
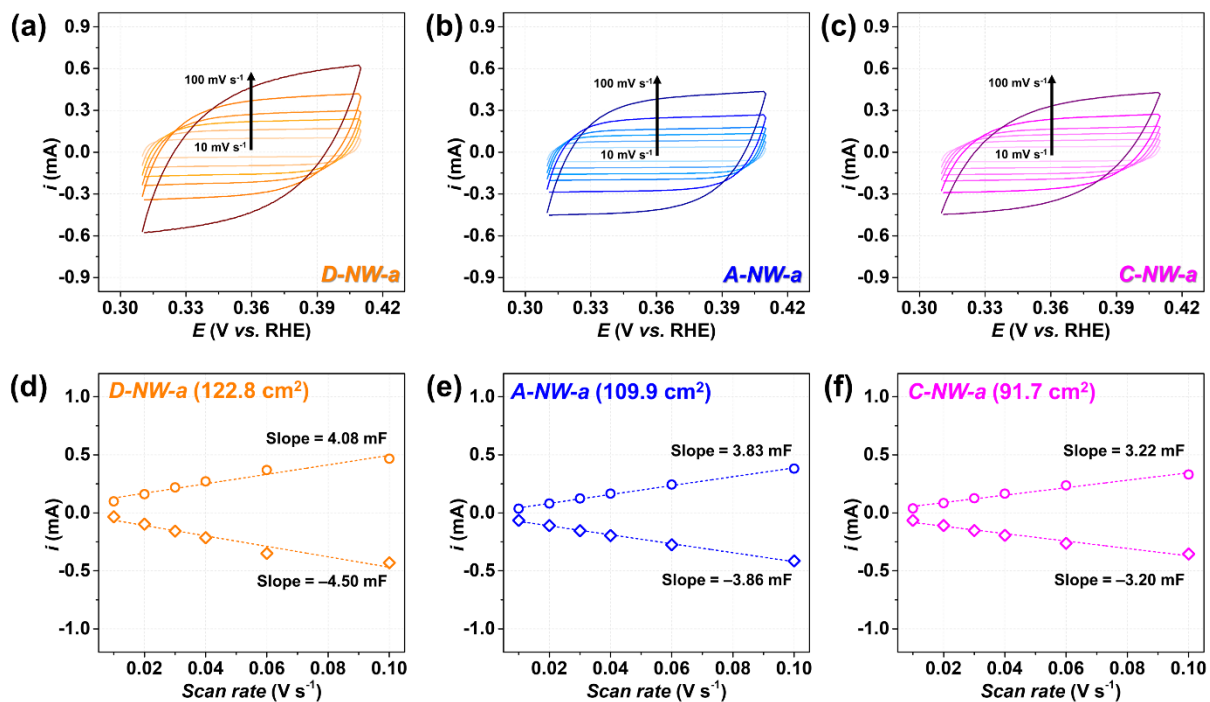
**Fig. S26.** Electrochemically active surface area (ECSA) by measuring double layer capacitances. (a-c) CV scans at different scan rates (10, 20, 30, 40, 60, and 100 mV s$^{-1}$) for (a) D-NW-a, (b) A-NW-a, and (c) C-NW-a, respectively. (d-f) Anodic and cathodic charging currents measured at 0.36 V$_{RHE}$ as a function of scan rate to measure double layer capacitances of the catalysts; (d) D-NW-a, (e) A-NW-a, and (f) C-NW-a.
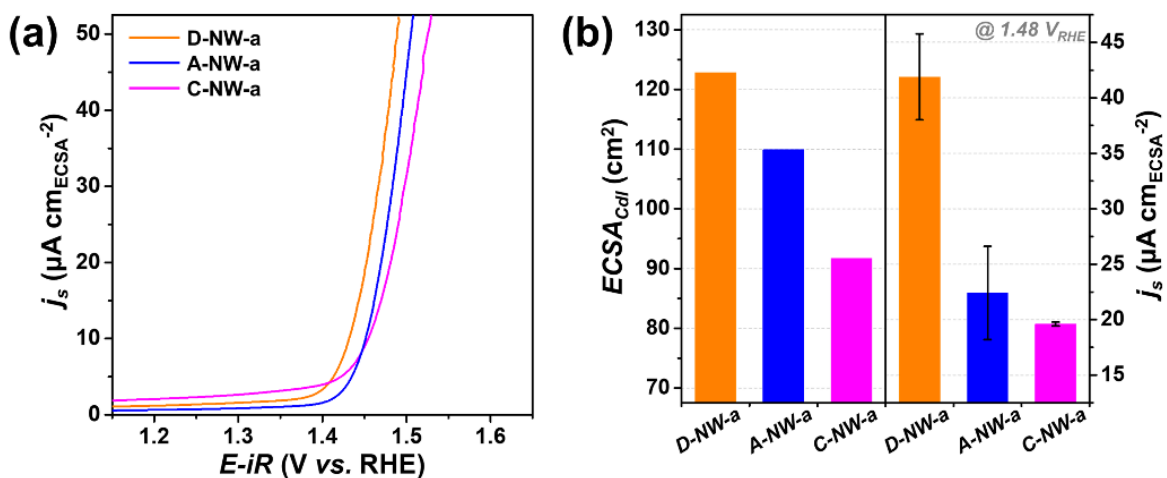
**Fig. S27.** (a) OER specific activity curves of the catalysts normalized by OER polarization curves (Fig. 4a) with the ECSA. (b) Comparison of ECSAs of the catalysts by double layer capacitances and corresponding specific activities of the catalysts at 1.48 $V_{RHE}$, normalized by ECSA.



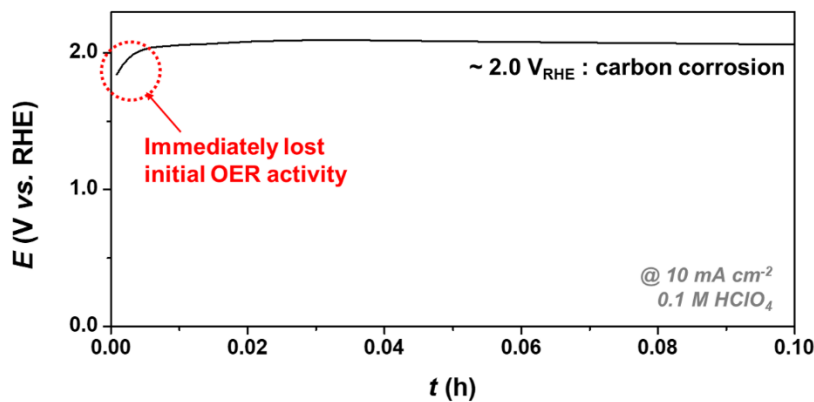**Fig. S28.** CP curves of the $RuO_2/C$ catalysts in $N_2$-saturated 0.1 M $HClO_4$ at a constant current density of 10 mA $cm^{-2}$. Constant voltage above 2.0 $V_{RHE}$ originate from carbon corrosion, not OER $RuO_2/C$.[S15-S16]
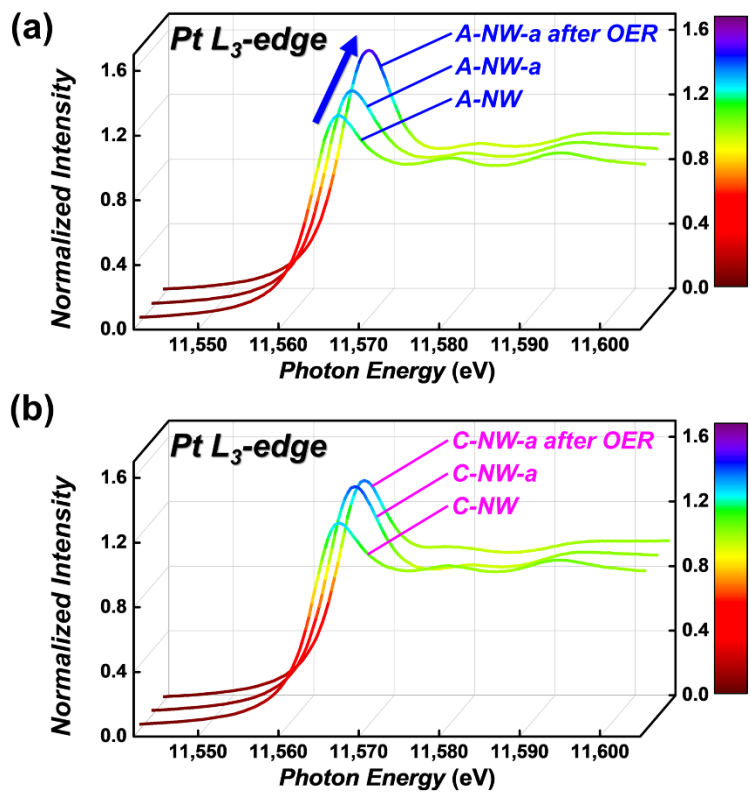
**Fig. S29.** (a) Pt L$_3$-edge XANES spectra of A-NW, A-NW-a, and A-NW-a after OER (CP test for 5 h). (b) Pt L$_3$-edge XANES spectra of C-NW, C-NW-a, and C-NW-a after OER.
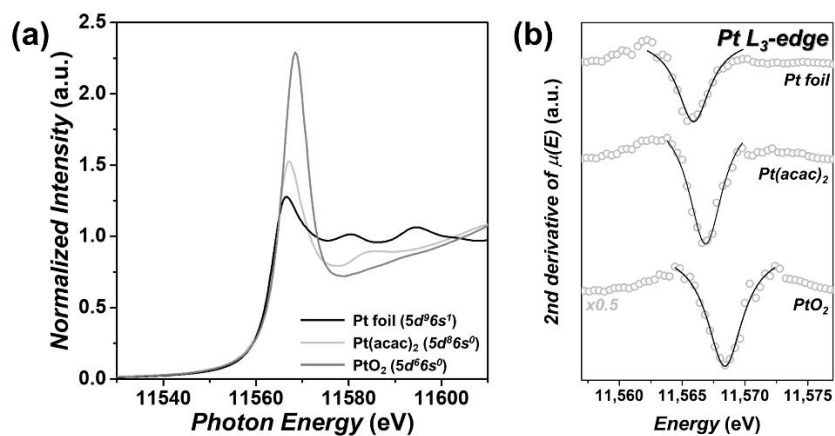
**Fig. S30.** (a) Pt L$_3$-edge XANES spectra of the reference materials; Pt foil (5d$^9$6s$^1$), Pt(acac)$_2$ (5d$^8$6s$^0$), and PtO$_2$ (5d$^6$6s$^0$). (b) Second derivatives of Pt L$_3$-edge XANES regions of Pt foil, Pt(acac)$_2$, and PtO$_2$ to determine white line position.
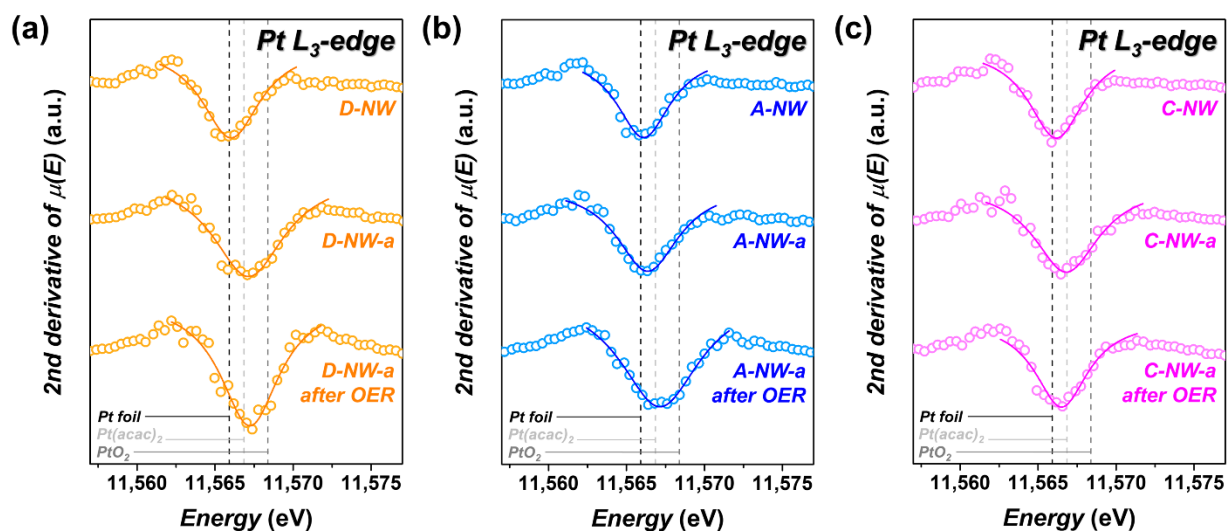


**Fig. S31.** Second derivatives of Pt L$_3$-edge XANES regions of the catalysts: (a) D-NW, D-NW-a, and D-NW-a after OER. (b) A-NW, A-NW-a, and A-NW-a after OER. (c) C-NW, C-NW-a, and C-NW-a after OER.
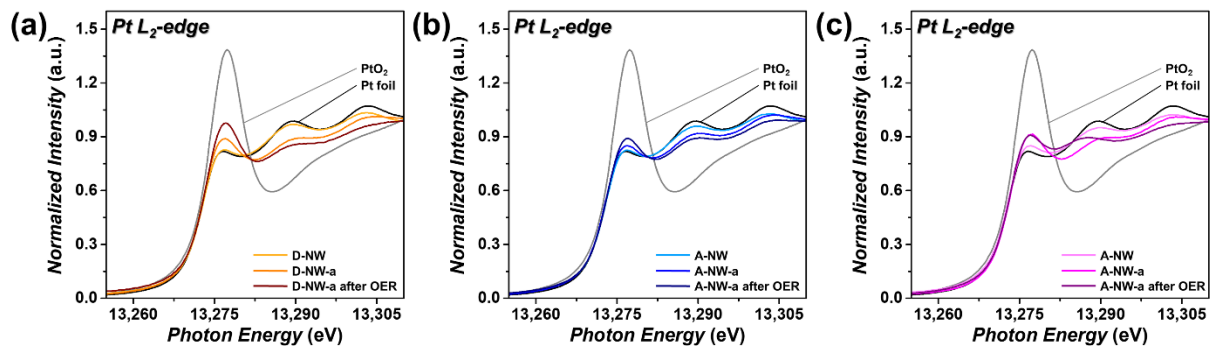
**Fig. S32.** Pt $L_2$-edge XANES spectra of the NW, NW-a, and NW-a after OER (CP test for 5 h); (a) D-NW and D-NW-a, (b) A-NW and A-NW-a, and (c) C-NW and C-NW-a, respectively. Pt foil and $PtO_2$ are also plotted as references.
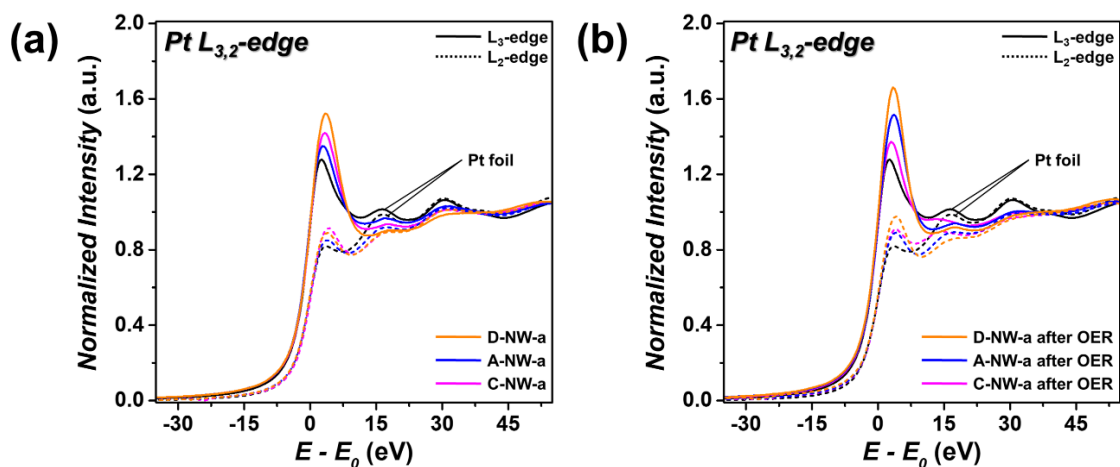


**Fig. S33.** Comparison of Pt $L_3$-edge (solid line) and Pt $L_2$-edge (dashed line) XANES spectra of NW-a catalysts (a) before and (b) after OER (CP test for 5 h). Pt foil is also plotted as reference.
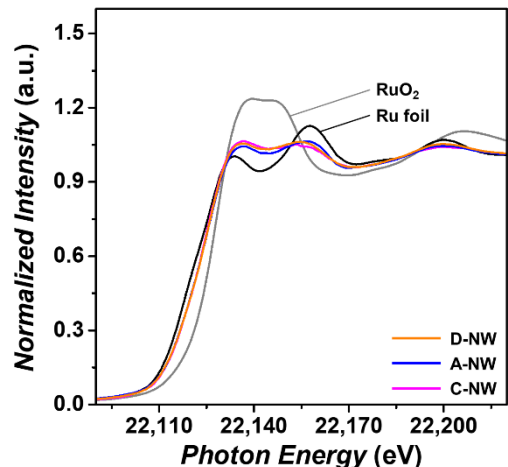
**Fig. S34.** Ru K-edge XANES spectra of the D-NW, A-NW, and C-NW. Ru foil and $RuO_2$ are also plotted as references.
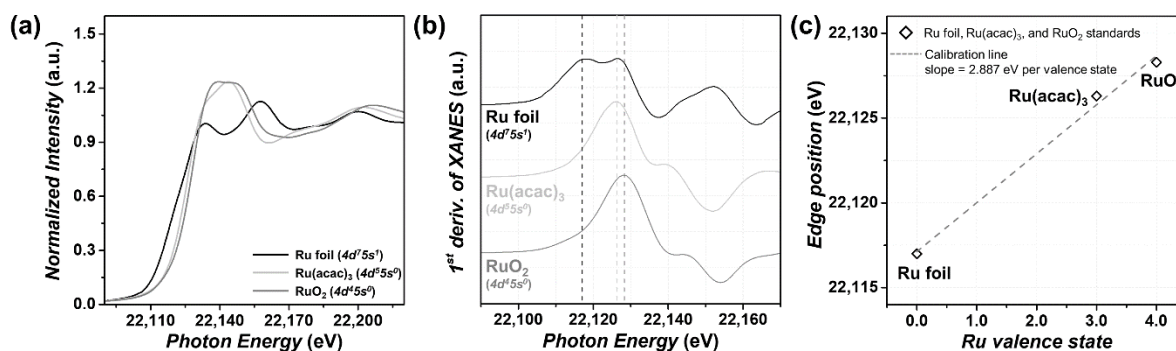


**Fig. S35.** (a) Ru K-edge XANES spectra of the reference materials; Ru foil ($4d^7 5s^1$), $Ru(acac)_3$ ($4d^5 5s^0$), and $RuO_2$ ($4d^4 5s^0$). Circles in the XANES spectra represents the edge position ($E_0$) measured from first derivatives of the XANES spectra. (b) First derivatives of Ru K-edge XANES spectra of Ru foil, $RuCl_3$, and $RuO_2$ to measure edge position. (c) Edge position of Ru foil, $RuCl_3$, and $RuO_2$ as a function of the Ru valence state. Ru valence states were calculated based on the Ru valence state and the increase of 2.887 eV per valence state.
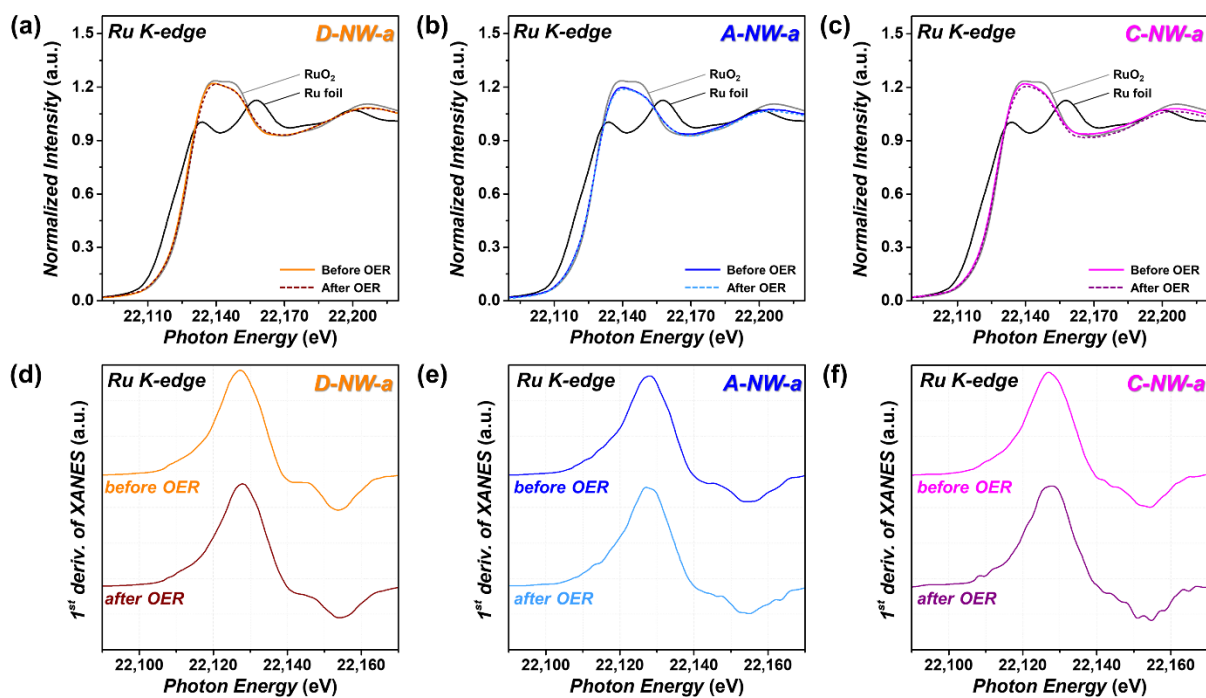
**Fig. S36.** (a-c) Ru K-edge XANES spectra of the NW-a catalysts before and after OER (CP test for 5 h); (a) D-NW-a, (b) A-NW-a, and (c) C-NW-a, respectively. Ru foil and $RuO_2$ are also plotted as references. (d-f) First derivatives of Ru K-edge XANES spectra of the catalysts before and after OER to determine the edge position. (d) D-NW-a, (e) A-NW-a, and (f) C-NW-a, respectively.
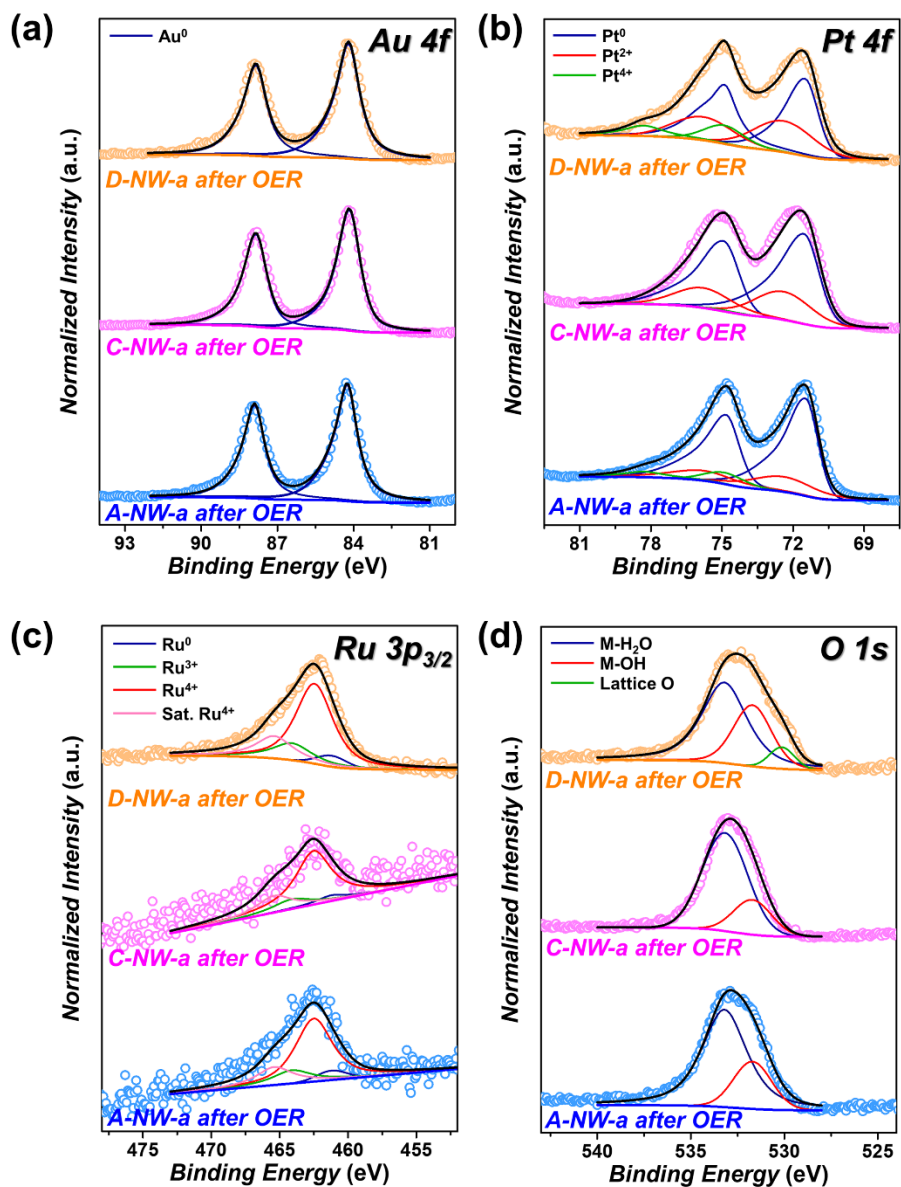
**Fig. S37.** (a) Au 4f, (b) Pt 4f, (c) Ru 3p$_{3/2}$, and (d) O 1s XPS spectra of D-NW-a, C-NW-a, and A-NW-a after OER (CP test for 5 h).
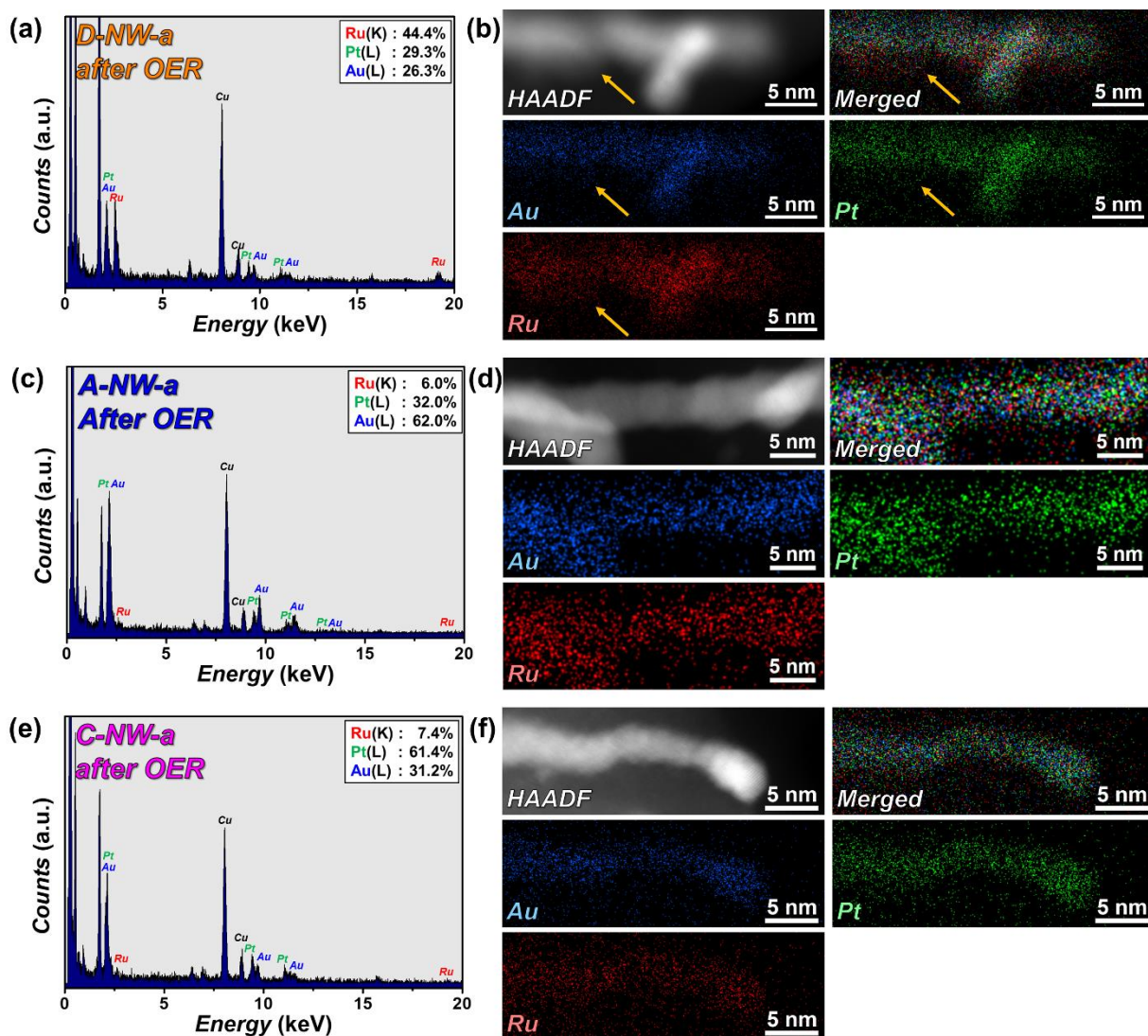
**Fig. S38.** (a,c,e) EDX spectra and (b,d,f) HAADF-STEM images and corresponding elemental mapping analyses of Au (blue), Pt (green), and Ru (red) contents in the NW-a catalysts after OER; (a,b) D-NW-a, (c,d) A-NW-a, and (e,f) C-NW-a, respectively. The yellow arrow in the panel (b) indicates the presence of hetero-structured $RuO_2$ phase on Au@Pt nanowires after OER.
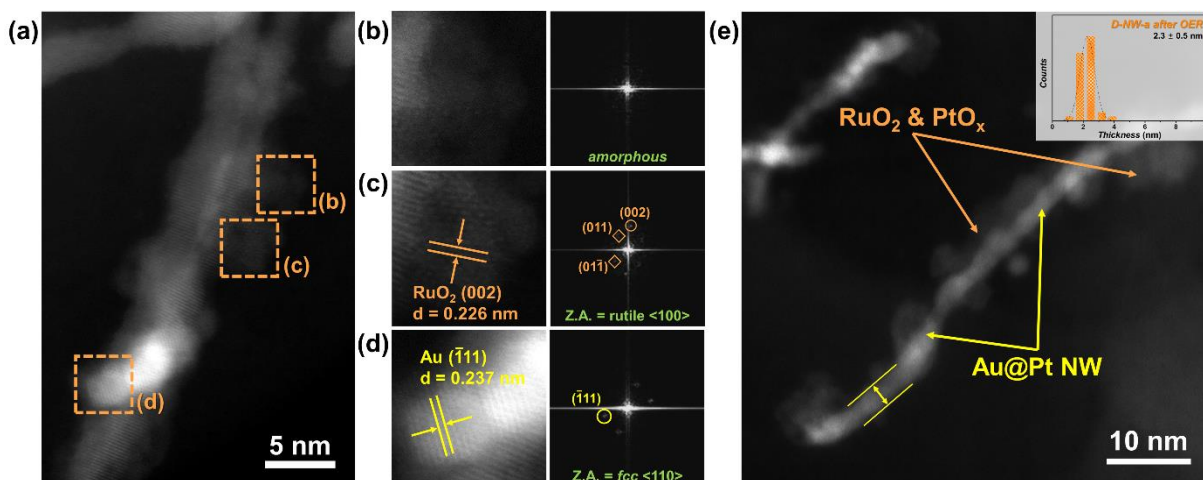
**Fig. S39.** (a) HR-STEM image of D-NW-a catalyst after OER. (b-d) Enlarged HR-STEM images of marked area in the panel (a) and corresponding FFT patterns. (e) HAADF-STEM image of D-NW-a after OER (inset: thickness distribution histogram of nanowire part of D-NW-a after OER).
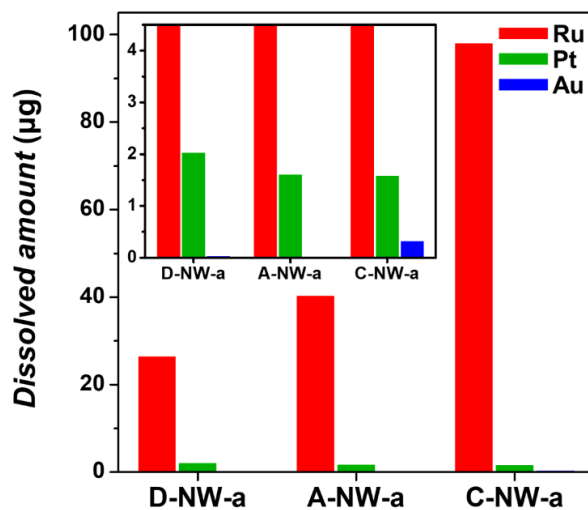


**Fig. S40.** Dissolved Au, Pt, and Ru contents of the catalysts after CP test for 5 h at 10 mA cm$^{-2}$ by measuring the electrolyte using ICP-MS. The CP test was conducted carbon paper electrode carbon paper ($1 \times 1$ cm$^2$, 100 $\mu g_{Ru}$ cm$^{-2}$) at a constant current density of 10 mA cm$^{-2}$.

# References in Supporting Information.

S1.    C. C. L. McCrory, S. Jung, I. M. Ferrer, S. M. Chatman, J. C. Peters, T. F. Jaramillo, *J. Am. Chem. Soc.*, 2015, **137**, 4347-4357.

S2.    B. Ravel, M. Newville, *J. Synchrotron Rad.*, 2005, **12**, 537-541.

S3.    A. Oh, H. Y. Kim, H. Baik, B. Kim, N. K. Chaudhari, S. H. Joo, K. Lee, *Adv. Mater.*, 2019, **31**, 1805546.

S4.    Y. Yao, S. Hu, W. Chen, Z.-Q. Huang, W. Wei, T. Yao, R. Liu, K. Zang, X. Wang, G. Wu, W. Yuan, T. Yuan, B. Zhu, W. Liu, Z. Li, D. He, Z. Xue, Y. Wang, X. Zheng, J. Dong, C.-R. Chang, Y. Chen, X. Hong, J. Luo, S. Wei, W.-X. Li, P. Strasser, Y. Wu, Y. Li, *Nat. Catal.*, 2019, **2**, 304-313.

S5.    J. Yi, W. H. Lee, C. H. Cho, Y. Lee, K. S. Park, B. K. Min, Y. J. Hwang, H.-S. Oh, *Electrochem. Commun.*, 2019, **104**, 106469.

S6.    L. Gloag, T. M. Benedetti, S. Cheong, Y. Li, X.-H. Chan, L.-M. Lacroix, S. L. Y. Chang, R. Arenal, I. Florea, H. Barron, A. S. Barnard, A. M. Henning, C. Zhao, W. Chuhmann, J. J. Gooding, R. D. Tilley, *Angew. Chem., Int. Ed.*, 2018, **57**, 10241-10245.

S7.    Y. Hu, X. Luo, G. Wu, T. Chao, Z. Li, Y. Qu, H. Li, Y. Wu, B. Jiang, X. Hong, *ACS Appl. Mater. Interfaces*, 2019, **11**, 42298-42304.

S8.    K. Wang, B. Huang, W. Zhang, F. Lv, Y. Xing, W. Zhang, J. Zhou, W. Yang, F. Lin, P. Zhou, M. Li, P. Gao, S. Guo, *J. Mater. Chem. A*, 2020, **8**, 15746-15751

S9.    J. Joo, H. Jin, A. Oh, B. Kim, J. Lee, H. Baik, S.H. Joo, K. Lee, *J. Mater. Chem. A*, 2018, **6**, 16130-16138.

S10.   J. Shan, T. Ling, K. Davey, Y. Zheng, S.-Z. Qiao, *Adv. Mater.*, 2019, **31**, 1900510.

S11.   J. Shan, C. Guo, Y. Zhu, S. Chen, L. Song, M. Jaroniec, Y. Zheng, S.-Z. Qiao, *Chem*, 2019, **5**, 445-459.

S12.   J. Xu, Z. Lian, B. Wei, Y. Li, O. Bondarchuk, N. Zhang, Z. Yu, A. Araujo, I. Amorim, Z. Wang, B. Li, L. Liu, *ACS Catal.*, 2020, **10**, 3571-3579.

S13.   X. Cui, P. Ren, C. Ma, J. Zhao, R. Chen, S. Chen, N.P. Rajan, H. Li, L. Yu, Z. Tian, D. Deng, *Adv. Mater.*, 2020, **32**, 1908126.

S14.   S. Laha, Y. Lee, F. Podjaski, D. Weber, V. Duppel, L.M. Schoop, F. Pielnhofer, C. Scheurer, K. Müller, U. Starke, K. Reuter, B.V. Lotsch, *Adv. Energy Mater.*, 2019, **9**, 1803795.

S15.  H.-S. Oh, H. N. Nong, T. Reier, M. Gliech, P. Strasser, *Chem. Sci.*, 2015, **6**, 3321-3328.

S16.  Y. Yi, G. Weinberg, M. Prenzel, M. Greiner, S. Heumann, S. Becker, R. Schlögl, *Catal. Today*, 2017, **295**, 32-40.